# Relative Abundance of $\mathbb{Z}_2$ Topological Order in Exfoliable Two-Dimensional Insulators

Antimo Marrazzo,[*,†] Marco Gibertini,[†,‡] Davide Campi,[†] Nicolas Mounet,[†] and Nicola Marzari[*,†]

[†]Theory and Simulation of Materials (THEOS) and National Centre for Computational Design and Discovery of Novel Materials (MARVEL), École Polytechnique Fédérale de Lausanne, 1015 Lausanne, Switzerland

[‡]Department of Quantum Matter Physics, University of Geneva, 24 Quai Ernest Ansermet, CH-1211 Geneva, Switzerland

*Supporting Information*

**ABSTRACT:** Quantum spin Hall insulators make up a class of two-dimensional materials with a finite electronic band gap in the bulk and gapless helical edge states. In the presence of time-reversal symmetry, $\mathbb{Z}_2$ topological order distinguishes the topological phase from the ordinary insulating one. Some of the phenomena that can be hosted in these materials, from one-dimensional low-dissipation electronic transport to spin filtering, could be promising for many technological applications in the fields of electronics, spintronics, and topological quantum computing. Nevertheless, the rarity of two-dimensional materials that can exhibit nontrivial $\mathbb{Z}_2$ topological order at room temperature hinders development. Here, we screen a comprehensive database we recently identified of 1825 monolayers that can be exfoliated from experimentally known compounds to search for novel quantum spin Hall insulators. Using density-functional and many-body perturbation theory simulations, we identify 13 monolayers that are candidates for quantum spin Hall insulators including high-performing materials such as $AsCuLi_2$ and (platinum) jacutingaite ($Pt_2HgSe_3$). We also identify monolayer $Pd_2HgSe_3$ (palladium jacutingaite) as a novel Kane-Mele quantum spin Hall insulator and compare it with platinum jacutingaite. A handful of promising materials are mechanically stable and exhibit $\mathbb{Z}_2$ topological order, either unperturbed or driven by small amounts of strain. Such screening highlights a relative abundance of $\mathbb{Z}_2$ topological order of around 1% and provides an optimal set of candidates for experimental efforts.

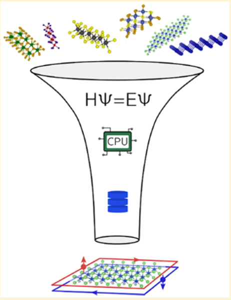

**KEYWORDS:** *Topological insulator, quantum spin Hall, two-dimensional material, high-throughput, first-principles*

Since the very first discovery of the quantum spin Hall insulating state in HgTe quantum wells in 2007,[1] the study of topological states of matter has seen enormous progress both in theory and experiments.[2] $\mathbb{Z}_2$ topological order, first discussed by refs 3, 4, and 5 for two-dimensional models, has also been formalized for three-dimensional materials,[6] leading to the discovery of the so-called “strong” and “weak” topological insulators. Although substantial progress has been made in predicting and confirming with experiments several three-dimensional topological insulators of different classes,[7] scant progress has been made in identifying their two-dimensional counterparts, that is, quantum spin Hall insulators (QSHIs). As of today, 1T′-$WTe_2$ is the only experimentally confirmed monolayer crystal hosting a robust QSHI phase up to 100 K;[8−10] considering more general systems, Bi on a SiC substrate stands out being a QSHI with a record-high measured band gap of 0.8 eV, owing to covalent bonding with the substrate.[11] In fact, two-dimensional (2D) materials also offer unique tunabilities offered by chemical[11] or strain[12] engineering driven by the substrate, surface passivation,[13,14] van der Waals heterostructures,[15] and more.[16]

Besides their fundamental scientific interest, several technological applications of topological insulators have been proposed. A broad class of these is based on using the one-dimensional topologically protected states at the edge of a QSHI to realize low-dissipation nanowires, where the elastic backscattering is forbidden by time-reversal (TR) symmetry and electron transport is spin-momentum locked.[2] For such applications, a large band gap would be beneficial not only to increase the operating temperature (limited by the intrinsic semiconducting behavior of the bulk) but also to decrease the transverse localization length of the edge states.[17] The latter could help to reduce inelastic backscattering with the bulk and, more relevantly, to suppress hybridization effects between the two pairs of helical states at opposite edges of a ribbon that otherwise would gap the edge spectrum. In the so-called topological field-effect transistor (TopoFET),[18] an out-of-plane applied electric field drives the system from a QSHI to a normal insulating phase and allows to switch on and off edge transport. It is clear that for TopoFETs applications, high-performance materials must exhibit an enhanced response to applied electric fields such that the topological phase transition occurs for realistic (i.e., sufficiently low) gate voltages. Coincidentally, a larger band gap typically implies a stronger QSHI phase and so larger critical fields for the topological phase transition. In addition, material-dependent effects, such

**Received:** July 2, 2019
**Revised:** October 7, 2019
**Published:** October 28, 2019

as thermal expansion or electron–phonon couplings, can also drastically affect the operating temperature of the device.[19,20] Hence, an accurate figure of merit for TopoFETs would include not only the zero-temperature band gap and band inversion but also a number of other quantities such as the critical electric fields or temperature of the topological phase transition, the stability with respect to oxidation, and the availability of good dielectric substrates. By looking at the current scenario, it is clear that the known QSHI materials present challenges for devices and applications, although examples like ref 11 (Bi on SiC) show that it is realistic and plausible to substantially increase performance through a combination of novel materials and careful engineering.

It is then compelling to seek for novel QSHI materials, possibly outperforming the state of the art. The optimal material might constitute a Pareto optimization that satisfies several requirements including, but not restricted to, those mentioned above. In this work, we use first-principles simulations to perform a systematic computational screening for QSHIs, using a combination of high-throughput density-functional theory (DFT) calculations, to first identify interesting candidates, and density-functional perturbation theory (DFPT) and many-body perturbation theory at the $G_0W_0$ level (with spin–orbit coupling (SOC)) to provide accurate predictions on the most interesting materials. The results of this screening not only provide a distilled set of this most promising QSHI candidates (several not reported before), that could orient experimental efforts, but they contribute to draw a comprehensive picture on the relative abundance and characterization of $\mathbb{Z}_2$ topological order in 2D materials.

**Screening Protocol.** We systematically explore 1825 two-dimensional (2D) materials coming from experimentally known, exfoliable compounds, searching for QSHIs. All these 2D materials were identified in ref 21 as easily or potentially exfoliable from their layered 3D parent crystals using extensive high-throughput first-principles calculations based on van der Waals DFT (vdW-DFT). Therefore, all the structures that we consider are known to exist at least in their bulk 3D form; we also note complementary approaches that suggested novel structures by decorating common structural prototypes for 2D materials with alternative, chemically similar elements.[22,23] Here, we select a set of computable properties defining good QSHIs candidates, and search the materials above in the hunt for novel QSHIs. In particular, we search for materials that are mechanically stable (i.e., whose phonons have no imaginary frequencies), that have a finite electronic band gap, a nonmagnetic ground state, and a nontrivial $\mathbb{Z}_2$ topological invariant. We adopt a computational high-throughput funnel approach (see Figure 1), where quantities that require less computational resources are computed first for the larger pool of structures, while more demanding properties are computed only for the progressively smaller sets of promising candidate materials. Given the manageable number of materials that we consider (of the order of thousands), we do not use approximate descriptors (as done earlier[24,25]), but we explicitly compute all properties from first principles. To begin with, we optimize the monolayer geometry (cell vectors and atomic positions) of all the structures in the set of ref 21 with an upper limit on the number of atoms in the unit cell, both for their higher relevance and for computational efficiency. Therefore, we restrict ourselves to all compounds containing no more than 30 atoms in the unit cell, for a total number of 1582 structures. Then lanthanides are removed, due to the limited accuracy of standard DFT in describing the electronic structures in such cases and the presence of multiple magnetic minima. The remaining compounds (1471 structures) are relaxed using the PBE functional assuming a nonmagnetic ground state, yielding successfully 1306 structures.[26] At this point, we compute band structures along high-symmetry lines using DFT and the PBE functional with SOC, selecting all the band insulators.[27] We compute the $\mathbb{Z}_2$ invariant for all these by tracking the evolution of hermaphrodite Wannier charge centers (HWCC),[28−30] as detailed in the Methods section. At this point, all insulators with a nontrivial $\mathbb{Z}_2$ invariant are considered tentative QSHIs, and we assess their mechanical stabilities by computing phonon dispersions (see Methods) using DFPT.[31]

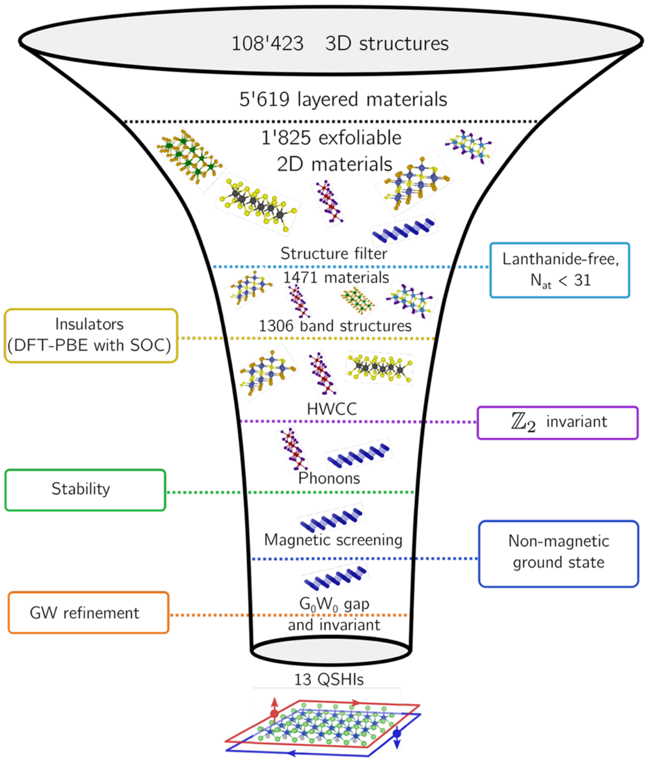

**Figure 1.** Computational protocol for the screening of quantum spin Hall insulators (QSHIs) exfoliable from experimentally known crystalline compounds. We start from the 1825 exfoliable 2D materials of ref 21, and each step reduces the number of potential candidates, with progressively more computationally intensive calculations. The high-throughput approach based on density functional theory calculations is complemented by density-functional perturbation theory and many-body perturbation theory calculations for the most interesting candidates. In particular, the topological phase is tested at the $G_0W_0$ level with spin–orbit coupling (SOC).

Although some recent work has focused on substituting the calculations of topological invariants with the use of descriptors[24,25,32] or with the elementary band representation,[33−35] we argue that the accuracy in the predictions of topological insulators is essentially driven by the accuracy of the calculated electronic structure and, in particular, of the spectral function. Substantial work has been made to find faster algorithms to compute the $\mathbb{Z}_2$ and other invariants, henceforth facilitating the calculation of such invariants in large data sets of crystalline materials[36−38] at a relatively low cost, essentially by maximally exploiting crystalline symmetries. However, for a reliable screening of topological insulators, most of the human and computational effort still goes into accurate band structure calculations (e.g., using $G_0W_0$ or dynamical mean field theory), in the study of possible magnetic ground states and in the assessment of mechanical stability (e.g., using phonons or molecular dynamics).[39]

By their very nature, topological insulators are characterized by topological invariants, that is, by integers that do not change under smooth deformations. Such a feature is often used as an argument in favor of the robustness of topological properties, the most spectacular cases being the quantization of the Hall conductance in the integer quantum Hall effect[40] and the robust presence of topological insulator surface states with respect to surface reconstruction or different terminations. The issue is how easy it is, in practice, to perform a nonsmooth deformation, which for a real material means to either break the protecting symmetries or close the gap. $\mathbb{Z}_2$ topological order is protected by time-reversal (TR) symmetry, and so the system must be non magnetic: any time-reversal breaking perturbation would destroy topological order without even necessarily closing the gap. Hence, we select only materials whose ground state is nonmagnetic based on the energetics of collinear DFT calculations for ferromagnetic and antiferromagnetic configurations (as in ref 21, see Methods).

Then the question is whether DFT self-interaction errors, correlation effects, inaccuracies in the structural properties, or approximating Dyson orbitals with Kohn−Sham (KS) states can be severe enough to affect the DFT topological classification. For TR-invariant topological insulators such as QSHIs, the topological phase is driven by a combination of crystal symmetries, hybridization, and SOC, and each of these aspects must be accurately treated to get reliable predictions. Broadly speaking, the most significant approximation is using the KS states that underestimate the gap and often overestimate the strength of the band inversion, leading to possible false negatives (discarding as metals materials that are insulating) or false positive (predicting topological insulators that are actually trivial band insulators).[41] SOC is typically sufficiently well described by semilocal DFT, in particular when the band gap opening is driven by atomic SOC,[42] although quantitatively less accurately when SOC enters as a hopping term.[43] For these reasons, at the last stage of our protocol we perform $G_0W_0$ calculations with the full nonperturbative treatment of SOC.[75,76]

Crystal symmetries are crucial and most predicted QSHIs actually fall in very few structural prototypes, such as the honeycomb lattice[44] or the distorted 1T′ phase of transition-metal dichalcogenides.[18,45] Recently, refs 34 and 35 emphasized the importance of site-symmetry groups, which impose strong constraints on the allowed connections between bands and hence determine the presence or absence of disconnected elementary band representations (i.e., topologically nontrivial manifolds) around the Fermi level. Hence, it is very important to adopt a crystal structure that faithfully represents the experimental structure at least at low temperatures, where vibrational effects can be neglected.[46] In this regard, our monolayer structures undergo a series of structural optimizations that initially starts from the bulk structures as obtained from experiments, and we note that the vast majority of known exfoliable 2D materials inherit the crystal symmetries of their parent 3D layered crystal and do not undergo structural transitions in the monolayer limit.

Nonetheless, ref 41 highlighted how sensitive $\mathbb{Z}_2$ topological order is with respect to the equilibrium lattice constant. As mentioned above, in the database of ref 21, we always started from experimental crystal structures and perform a first structural optimization using vdW-DFT; once identified as exfoliable, we perform a second structural optimization for the monolayers using DFT-PBE. The structural optimization of a selected subset of 258 easily exfoliable compounds with at most 6 atoms per unit cell is discussed in ref 21, while here we have extended it to the rest of the database to screen for QSHIs. For materials that are identified as prospective QSHI candidates, we perform an additional structural optimization with tighter thresholds and more accurate, more computationally expensive, pseudopotentials (see Methods). Although we pay particular attention to structural optimizations, we also monitor deviations between the experimental and the calculated equilibrium lattice constants. Hence, we augment our protocol by considering all metals with a direct gap (DGM) along high-symmetry paths (built following ref 47) and apply a ± 1, 2, 3% hydrostatic strain (see Methods). DGMs are chosen because they can be adiabatically connected to the insulating state and the $\mathbb{Z}_2$ invariant can be well-defined considering the first $n_e$ bands where $n_e$ is the number of electrons, even if the Fermi level does not lie in a gap. If a DGM becomes an insulator under strain, then the strained structure is added to the list of materials to be screened for QSHIs. This procedure has the two-fold purpose of identifying materials that would be QSHIs at their experimental lattice constant or that could be driven to be QSHI, for example, by choosing a suitable substrate. There could still be systems that would not become insulators under strain at the DFT-PBE level and yet be insulators experimentally and recognized as such by, for example, many-body perturbation theory. Although such materials can exist and may even display robust band inversions, it is unlikely that they would have very large band gaps, hence given the very high computational cost we leave such investigation to future work.

Finally, we address correlation effects by performing as mentioned (very costly) many-body perturbation theory calculations ($G_0W_0$ with SOC) for the five most interesting QSHI candidates. These materials have been chosen as optimal in the sense they optimize the multidimensional requirements of low binding energies, large electronic band gaps, and strong band inversions. Some of them excel for certain aspects (e.g., large band gap) while keeping a sufficiently good performance on all the other relevant parameters or because they show a good average over all parameters without being the top material in any of the quantities considered.

Although the suppression of bulk transport is inherently related to the size of the global band gap, the robustness of the topological phases is mostly dictated by the magnitude of the band inversion. To be more precise, we define the inversion strength (IS) for the two classes of QSHIs. For Bernevig-Hughes-Zhang (BHZ) QSHIs,[48] where there is a clear band inversion between electronic bands of different orbital character, the IS is defined as the energy difference between the lowest unoccupied and the highest occupied band at the high-symmetry point where the band inversion occurs (e.g., Γ for Bi monolayers). For Kane-Mele QSHIs, where a single Dirac cone at K is gapped by the Kane-Mele SOC,[3,4] we define the IS as the direct band gap at K. Hence, we compute the inversion strength both at the DFT-PBE and $G_0W_0$ levels with SOC by evaluating the direct gap at the relevant high-

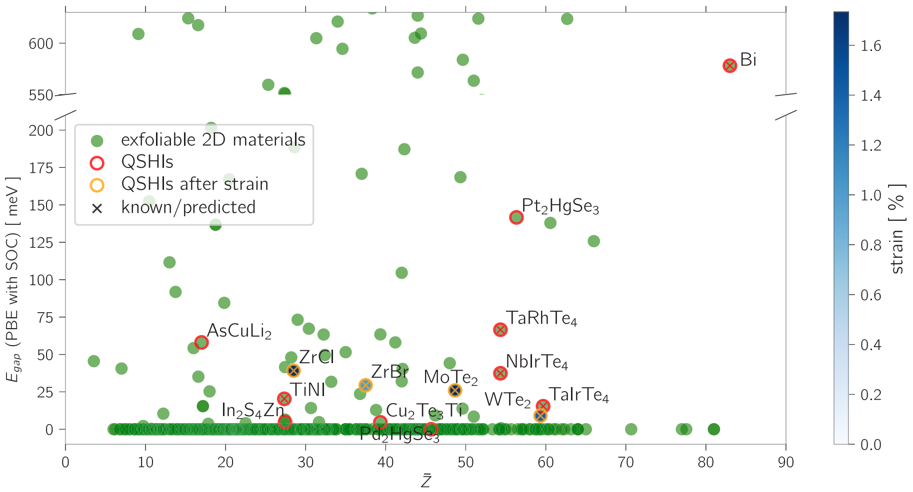

**Figure 2.** Band gap at the DFT-PBE level with SOC versus average atomic number for several exfoliable 2D materials identified in ref 21. QSHI candidates are denoted by red circles; strain-driven QSHIs are marked by orange circles and colored according to the minimum amount of strain to open a band gap. We identify 13 candidates (5 new) out of the 1306 screened, to which we add palladium jacutingaite ($Pd_2HgSe_3$), recently synthesized,[54] as the second ever KM QSHIs.

**Table 1. QSHI Candidates and Their Corresponding Properties**[a]

| compound | space group | $E_b$ [meV Å$^{-2}$] (DF2-C09/rVV10) | band gap PBE [meV] | inversion strength PBE [meV] | inversion strength $G_0W_0$ [meV] | strain [%] | QSHI type | ref |
|---|---|---|---|---|---|---|---|---|
| Bi | $P\bar{3}m1$ (164) | 18/25 | 545 | 685 | 760 | none | BHZ | 21 |
| $Pt_2HgSe_3$ | $P\bar{3}m1$ (164) | 60/63 | 149 | 168 | 530 | none | KM | 43 |
| $Pd_2HgSe_3$ | $P\bar{3}m1$ (164) | 61/66 | 0 | 80 | 41 | none | KM | 54 |
| TiNI | $Pmmn$(59) | 15/22 | 18 | 141 | −705 (trivial) | none | BHZ | 21,51 |
| $AsCuLi_2$ | $P\bar{6}m2$ (187) | 63/62 | 45 | 80 | 169 | none | BHZ | |
| $WTe_2$ | $P2_1/m$ (11) | 30/27 | 9 (2%) | 972 | 978 (from 18) | 2% | BHZ | 18,21 |
| $MoTe_2$ | $P2_1/m$ (11) | 25/30 | 26 (3%) | 408 | 403 (from 18) | 3% | BHZ | 18,21 |
| $TaIrTe_4$ | $Pm$ (6) | 26/31 | 11 | 204 | | none | BHZ | 45 |
| $TaRhTe_4$ | $Pm$ (6) | 26/31 | 65 | 215 | | none | BHZ | 45 |
| $NbIrTe_4$ | $Pm$ (6) | 27/32 | 36 | 161 | | none | BHZ | 45 |
| $Cu_2Te_3Ti$ | $C2/m$ (2) | 44/44 | 8 | 21 | | none | BHZ | |
| $In_2ZnS_4$ | $P3m1$ (156) | 36/39 | 0 | 191 | | none | BHZ | |
| ZrBr | $P\bar{3}m1$ (164) | 16/22 | 29 (1%) | 45 (1%) | | 1% | BHZ | 52,53 |
| ZrCl | $P\bar{3}m1$ (164) | 15/22 | 39 (3%) | 60 (3%) | | 3% | BHZ | 53 |

[a] Chemical formula, space group, binding energy computed with two different van der Waals functionals (DF2-C09 and rVV10, see Methods), band gap at the DFT-PBE level with SOC, inversion strength at the DFT-PBE level with SOC, inversion strength at the $G_0W_0$ level with SOC, minimum amount of strain to be insulating (DFT-PBE level), topological phase type (either Kane-Mele or Bernevig-Hughes-Zhang), reference (if present).

symmetry point. $G_0W_0$ calculations of 2D materials are known to be very challenging in terms of computational resources due to the strong dependence of the 2D dielectric function around $\mathbf{q} = 0$.[49,50] We provide an accurate estimate of the band inversion by using a series of very dense **k**-point grids (e.g., up to 48 × 48 × 1 or more) and extrapolate to an infinitely dense grid (see Methods).

**Results.** The results of the computational screening are summarized in Figure 2 and in Table 1. We find 13 QSHIs candidates using the protocol described above; these are listed in Table 1, together with key relevant properties: their space group, binding energy, band gap, inversion strength, underlying model (BHZ or KM), minimum amount of strain to drive an insulating topological phase, and relevant references if present. In addition, we present in the Supporting Information the crystal structures, the DFT-PBE band structures (with and without SOC), the DFPT phonon dispersions (without SOC, except for jacutingaite), and the evolution of the HWCC (determining the $\mathbb{Z}_2$ invariant) for each of these candidates. In Figure 2, we report the band gap at the DFT-PBE level versus the average atomic number of a given crystal structure for all the screened materials whose band gap is in a relevant energy range. All compounds are identified by a green disk, and QSHI candidates (at the DFT-PBE level) are marked with an additional red circle. In case the QSHI phase is driven by strain, the structure is marked by an orange circle, and the disk is colored in blue according to the minimum amount of strain that is necessary to drive a transition from the metallic to the insulating state (essentially opening an indirect band gap).

As expected, all candidates are essentially narrow gap semiconductors, with band gaps lower than 0.6 eV driven by SOC. Apart from the obvious observation that SOC is due to the presence of heavy chemical elements, there is no strong correlation between the magnitude of the band gap and the highest or average atomic number for the atoms of a given structure. However, the two largest-gap candidates, namely Bi and $Pt_2HgSe_3$, indeed contain three of the heaviest non-radioactive elements of the periodic table (Pt, Hg, Bi). In

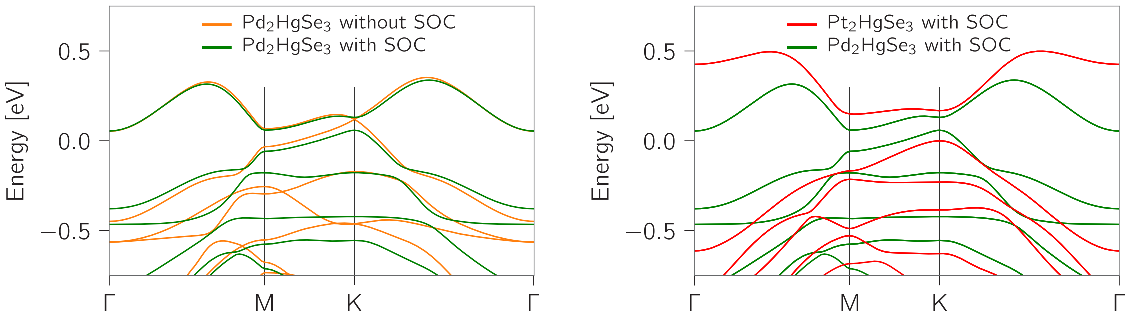

**Figure 3.** Left panel: DFT-PBE band structure with (green) and without (orange) SOC for monolayer $Pd_2HgSe_3$, where a Dirac crossing at K is gapped by SOC, as in monolayer $Pt_2HgSe_3$. Right panel: DFT-PBE band structure with SOC for monolayer $Pd_2HgSe_3$ (green) and monolayer $Pt_2HgSe_3$ (red); the large band gap of the latter is driven by the presence of the heavy element Pt.

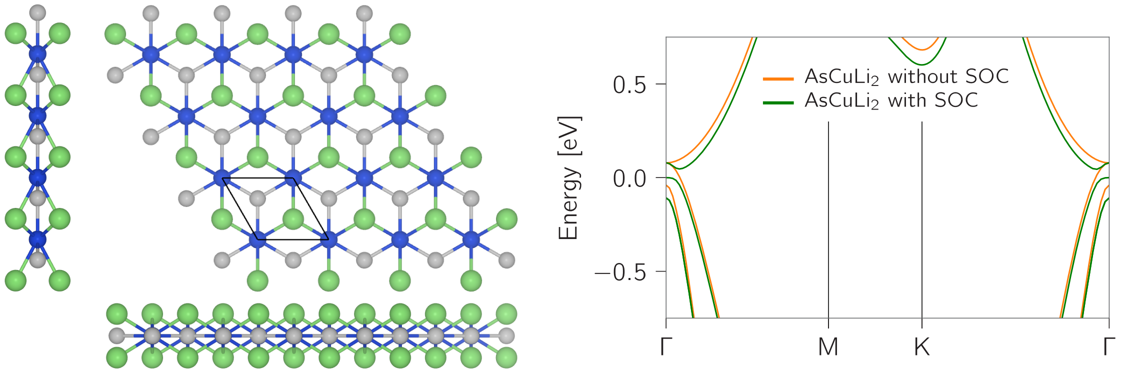

**Figure 4.** Left panel: Crystal structure of $AsCuLi_2$ (top and lateral views), a potentially exfoliable material identified in ref 21. Right panel: DFT-PBE band structure with (green) and without (orange) SOC for monolayer $AsCuLi_2$, where SOC drives a band inversion at Γ.

addition to the exfoliable materials of ref 21, we added $Pd_2HgSe_3$ (palladium jacutingaite), which was not included in ICSD or COD at the time the study of ref 21 was performed. $Pd_2HgSe_3$ is a crystalline compound that has recently been identified experimentally[54,55] and whose structure is identical to (platinum) jacutingaite ($Pt_2HgSe_3$) and is also potentially exfoliable with a very similar binding energy (~60 meV $Å^{-2}$, see Table 1). We now first discuss individually the most interesting candidates and then comment on some trends.

*Bi.* Monolayer bismuth has long been predicted to be a QSHI,[56] although experimental confirmation has proven to be difficult,[57−59] and the isolation of a clean monolayer is still a challenge. With a very low binding energy (~20 meV $Å^{-2}$), a strong band inversion (0.7 and about 0.8 eV at the PBE and $G_0W_0$ level, respectively), and very large band gap (~0.6 eV with PBE), monolayer bismuth remains a very interesting candidate. Monolayer bismuth is a unary compound with a relatively simple crystal structure, namely a buckled honeycomb lattice with two atoms per unit cell, that makes it appealing also from the point of view of experimental synthesis. Indeed, a recent experimental effort reported that Bi on a SiC substrate is a record-high QSHI with a 0.8 eV band gap, although the covalent bonding substantially alters the atomic and electronic structure of the monolayer.[11]

*$Pt_2HgSe_3$/$Pd_2HgSe_3$.* Platinum jacutingaite ($Pt_2HgSe_3$) and palladium jacutingaite ($Pd_2HgSe_3$) share very similar band structures (see Figure 3). They are the first, and currently only, two exfoliable materials that realize the Kane-Mele model with a Dirac cone at K split by SOC, although they also exhibit some differences. $Pd_2HgSe_3$ is metallic at the level of DFT-PBE: although SOC opens a gap at K, the bottom of the conduction band (at Γ) is degenerate with the top of the valence band (at K), giving a band-overlap semimetal with a finite direct gap at each **k**-point. $G_0W_0$ quasiparticle corrections open a gap and show that monolayer $Pd_2HgSe_3$ is a Kane-Mele QSHI, with a band inversion estimated from extrapolations to be around 41 meV (much smaller than the 0.5 eV of $Pt_2HgSe_3$[43]). In addition, the direct gap at K is roughly a third (0.07 eV with PBE) of the one of jacutingaite (0.17 eV with PBE); this is perfectly consistent with the analysis of ref 43, where 2/3 of the gap at K of jacutingaite is attributed to Pt and only a third to Hg. As mentioned, these are the only two QSHI candidates of the Kane-Mele type we found (in addition to graphene itself which is not included here owing to its vanishing small band gap).

*TiNI.* With a very low binding energy (~20 meV $Å^{-2}$), a good inversion strength (0.17 eV with PBE), and sufficient band gap (0.03 eV with PBE), TiNI may seem a good candidate, and indeed it has already been identified independently by different authors[21,51] as a QSHI. However, $G_0W_0$ calculations point to TiNI actually having a trivial character with a relatively large direct gap at Γ of 0.7 eV, and with no band inversion, so previous suggestions should be discounted. Such finding highlights the fundamental importance of performing accurate quasiparticle calculations when predicting topological phases,[41] especially for 2D materials where the dielectric screening is weak and the dielectric function has a strong spatial dependence.[49,50]

*$AsCuLi_2$.* This is a promising QSHI candidate, never reported before, with a good band inversion (0.08 eV with PBE) that gets actually stronger at the $G_0W_0$ level (0.17 eV) and a sufficient band gap (0.06 eV at the PBE level). The

crystal and band structures of monolayer $AsCuLi_2$ are reported in Figure 4. The crystal structure can be decomposed into a honeycomb lattice made of As and Cu (as in hexagonal boron-nitride) sandwiched between two triangular lattices made of Li; the two Li sublattices sit above and below the mirror plane represented by the AsCu sublattice. This is a novel structural prototype for QSHIs, with space group 187 and characterized by a clean band inversion at Γ. At the DFT-PBE level without SOC, the system is a filling-enforced semimetal, that is, the Fermi surface displays nodal features at specific electron fillings that are protected by a combination of crystalline and time-reversal symmetries, characterized by a symmetry-protected four-fold degenerate point at Γ. The orbital character of the Fermi surface is a combination of $d_{x^2-y^2}$, $d_{xy}$ orbitals of Cu and $p_x$, $p_y$ orbitals of As. Here SOC gaps the four-fold degeneracy point and opens an indirect gap, owing to the presence of the heavy element As.

*W(Mo)Te₂.* Transition metal dichalcogenides in the 1T′ phase have been predicted to host robust QSHI phases,[60] with several experimental confirmations for the case of $WTe_2$.[8−10] On the computational side, the strong band inversion of $WTe_2$ is present at different levels of theory, from PBE[60] to HSE[8,61] to $G_0W_0$.[60] However, the evidence of a strictly insulating bulk with a finite band gap is extremely sensitive to the lattice constant and the techniques used to compute the band structure, where a finite gap appears with the HSE functional, while no indirect gap is present with PBE and $G_0W_0$. At the PBE level, a small compressive strain (2%) is enough to open a global gap. $WTe_2$ has a low binding energy (~30 meV Å$^{-2}$), and it is known to be exfoliable with scotch-tape techniques.[10] Among the QSHIs we find, $WTe_2$, currently considered the best monolayer QSHIs, is not studied in detail here as it has been thoroughly discussed in the recent experimental and theoretical literature.[8−10,18]

*MM′Te₄.* Monolayers of the MM′ class of tellurides, where M = Nb, Ta and M′ = Ir, Rh, had already been proposed in ref 45 and confirmed here to host the QSHI phase. The crystal structure is similar to the 1T′ phase of $WTe_2$, with W atoms replaced alternatively by distinct transition metals M and M′. Their low binding energy and good band inversion (up to ~0.2 eV in $TaRhTe_4$) make them good candidates for experimental studies.

*In₂ZnS₄.* In addition to potentially novel high-performance QSHI candidates, the computational screening provides also novel ideas and prototypes that would possibly inspire the engineering of materials, with $In_2ZnS_4$ being an excellent example. $In_2ZnS_4$ is a potentially exfoliable material ($E_b \approx 35$−40 meV Å$^{-2}$) with a good band inversion and a vanishing small band gap, overall a not-so promising QSHI candidate. However, $In_2ZnS_4$ has a very peculiar crystal structure that could be thought of as being made of two separate 2D subunits, partially bonded together by van der Waals interactions. In fact, to properly refine the crystal structure, we further optimize it by using a nonlocal vdW functional (DF2-C09,[62,63] see Methods). The case of $In_2ZnS_4$ suggests the possibility of stacking monolayers with moderate interactions to engineer a topological phase, where the strength of the interactions is stronger than in simple vdW heterostructures and substantially weaker that in the case of Bi on a SiC substrate.[11] To this aim, one could explore all the possible combination of the ~1000 potentially exfoliable materials identified in ref 21.

*ZrBr(Cl).* In these materials, the QSHI phase, typically driven by crystal field and marked by relatively small band inversions with small or even vanishing indirect band gaps, is very sensitive to the lattice constant.[41] This can potentially be exploited by substrate engineering, where the choice of a suitable close-matched substrate can strain the monolayer and drive a QSHI phase. At the DFT-PBE level, ZrBr has a small band inversion, and it is just on the edge of being an insulator, with an indirect gap that opens already at 1% of isotropic strain. ZrCl has the same prototype of ZrBr, although it requires a little bit more strain (3%) to open a band gap.

Although the limited number (13) of QSHI candidates does not allow the use of statistics, it is worth mentioning that one-third of all candidates have a crystal structure with space group $P\bar{3}m1$ (164) and all candidates have less than 12 atoms per unit cell (our search was conducted on all exfoliable materials with up to 30 atoms per unit cell). This hints at a possible correlation between the presence of a QSHI phase and particular structural motifs or specific point groups in small crystal structures, and it will be studied in future work. In addition, the presence of very heavy elements such as Bi, Hg, and Pt (and probably Pb[23]) seems to be beneficial for large band gaps, independently of the precise mechanisms through which SOC opens a band gap.

**Conclusions.** Using a combination of high-throughput DFT techniques and accurate DFPT and MBPT-$G_0W_0$ calculations, we have screened 1306 out of 1825 exfoliable two-dimensional materials proposed in ref 21 to search for novel QSHIs. We have identified 13 monolayers as dynamically stable and easily/potentially exfoliable QSHIs. By using the high-throughput protocol described here, we identify several compounds that have already been predicted as QSHIs (e.g., $TaRhTe_4$ or TiNI) and, in a few cases, also confirmed with experiments (Bi, $WTe_2$), validating the approach. In addition, we found several novel candidates, including promising high-performance materials such as $AsCuLi_2$, a second Kane-Mele QSHI $Pd_2HgSe_3$ or inspiring novel prototypes such $In_2ZnS_4$. We also showed the importance of adopting accurate theoretical frameworks to deal with SOC and excited states, which can dramatically affect the prediction of topological phases; this is most remarkable in the case of TiNI, predicted to be a QSHI by DFT-PBE calculations and found here to be trivial at the level of $G_0W_0$. This screening effort points to a relative abundance of $\mathbb{Z}_2$ topological order in two-dimensional insulators of around 1%. We want to remark that this does not imply that topological order is a rare property; at least for 3D materials this has been shown not to be the case,[35] with a sizable fraction of all crystals showing electronic manifolds that are topologically nontrivial in a broad sense.[36−38] What seems to be relatively rare is the simultaneous occurrence of a true 2D bulk insulating phase that exhibits $\mathbb{Z}_2$ topological order considering the entire manifold of the occupied valence bands, which phenomenologically coincides with the presence of strictly 1D electronic transport dominated by topologically protected helical edge states. We differentiate such systems, both topological and truly insulating, from the general case of metals with a well-defined interband gap where nontrivial topological invariants can be well-defined. In the latter case, topologically protected gapless edge states are superimposed to the gapless bulk energy spectrum; the entire system, bulk and terminations alike, behaves as a metal. As a matter of fact, only systems where the electron transport happens exclusively along the 1D topologically protected helical edge states can be of interest for devices and applications, allowing to exploit the absence of elastic backscattering, spin-momentum locking, and robustness to perturbations.

The present screening provides a useful set of promising and novel QSHI candidates that would ideally prompt further experimental efforts. All the relevant data on the materials we propose are also available on the Materials Cloud platform at https://materialscloud.org/discover/2dtopo/, where optimized crystal structures, electronic bands, phonons, and other properties are available for download and can be accessed interactively through the browser. Finally, we highlight that extensive computational materials screenings of this kind provide a unique advantage of finding unexpected novel prototypes and mechanisms that do not fit into the existing knowledge and could possibly inspire, as in the case of $In_2ZnS_4$, novel engineering strategies.

**Methods.** DFT calculations are performed with the Quantum ESPRESSO distribution,[64,65] using the PBE functional and the SSSP[66] and PseudoDojo[67,68] pseudopotentials libraries. The SSSP library[66] contains two sets of extensively tested pseudopotentials from various sources: the SSSP efficiency, tailored for high-throughput materials screening, and the SSSP precision, developed for high-precision materials modeling. As of today, the SSSP precision library is the most accurate open-source pseudopotential library available[66] compared to all-electron reference data[69] (together with VASP GW-ready pseudopotentials). For the SSSP library, wave function and charge-density cutoffs are chosen according to convergence tests with respect to cohesive energy, pressure, band structure, and phonon frequencies performed for each individual element, as discussed in ref 66. For the fully relativistic PseudoDojo library,[68] wave function cutoffs are chosen according to convergence tests with respect to the band structure of elemental crystals, in particular converging the $\eta_v$ and $\eta_{10}$ below 10 meV and max $\eta_v$ and the max $\eta_{10}$ below 15 meV, respectively (see ref 66). For the high-throughput calculations without (with) SOC, we use a **k**-point density of 0.2 Å$^{-1}$ using a Marzari-Vanderbilt smearing[70] of 0.02 Ry and the SSSP efficiency v1.0 (PseudoDojo) library. Structural optimization, band structures, and phonon dispersions are computed using scalar relativistic calculations without SOC using the SSSP library v1.0, band structure are also recomputed using fully relativistic calculations with SOC using the PseudoDojo library. Two exceptions are made, namely for monolayer TiNI where PseudoDojo pseudopotentials have been used both for the scalar and fully relativistic calculations, and for monolayer $In_2ZnS_4$ where we used the vdW-DF2 functional[62] with C09 exchange (DF2-C09)[63] for the structural optimization to take into account the effect of van der Waals interaction between the ZnS and $In_2S_3$ subunits. For the materials identified as band insulators, the subsequent fully relativistic calculations (e.g., to compute the $\mathbb{Z}_2$ invariant) are performed with fixed occupations. A refinement on structural optimization of the QSHIs candidates is performed using a **k**-point density of 0.1 Å$^{-1}$ and the SSSP precision v1.0 library.

The interlayer distance and $E_b$ are computed[21] using two different nonlocal van-der-Waals functionals: the vdW-DF2 functional[62] with C09 exchange (DF2-C09)[63] and the revised Vydrov-Van Voorhis (rVV10) functional.[71,72] Topological invariants are computed using Z2pack,[29,30] which exploits the hermaphrodite (a.k.a. hybrid) Wannier functions[28] that in 2D are defined as[30]

$$|n;\, l_x,\, k_y\rangle = \frac{a_x}{2\pi}\int_{-\pi/a_x}^{\pi/a_x} e^{ik_x l_x a_x}|\psi_{n\mathbf{k}}\rangle\, \mathrm{d}k_x \tag{1}$$

where $a_x$ is the lattice constant along the $x$ axis, $l_x \in \mathbb{Z}$. Hermaphrodite Wannier functions are Wannier-like in one direction and Bloch-like in the others, and the evolution of their centers across the BZ can be related to the Chern number,[29,30] in particular

$$C = \frac{1}{a_x}\left(\sum_n \bar{x}_n(k_y = 2\pi) - \sum_n \bar{x}_n(k_y = 0)\right) \tag{2}$$

where $\bar{x}_n$ are the charge centers defined as

$$\bar{x}_n(k_y) = \langle n;\, 0,\, k_y|r_x|n;\, 0,\, k_y\rangle = \frac{a_x}{2\pi}\int_{-\pi/a_x}^{\pi/a_x} A(k_x)\, \mathrm{d}k_x \tag{3}$$

with $A(k_x)$ being the Berry connection. Hence, the Chern number can be computed by tracking the evolution of the HWCC across the BZ and essentially counting their winding number. The $\mathbb{Z}_2$ topological invariant can be then obtained by splitting the Hilbert spaces into two sets, one the TR-conjugate of the other, and finally computing the Chern number for only one of the two. In practice, this means tracking the HWCC evolution on half of the BZ, through the algorithm introduced in ref 29.

Phonons dispersion have been obtained using DFPT[31] with a 2D Coulomb cutoff,[73,74] using the SSSP precision library v1.0 and a **q**-points mesh at least half as dense as the one used for the refinement (so roughly 0.2 Å$^{-1}$).

$G_0W_0$ calculations are performed with the Yambo code[75,76] on top of DFT-PBE calculations performed with Quantum ESPRESSO. For the Yambo calculations, we use fully relativistic ONCV pseudopotentials from the PseudoDojo library, using the GW version (with complete shell in the valence)[68] when available. In the $G_0W_0$ calculations, we adopt the random integration method (RIM),[75] the 2D Coulomb cutoff,[75] and the plasmon-pole approximation for the frequency dependence of the self-energy.[77,78] SOC is included self-consistently at the DFT level using spin−orbitals and fully taken into account at the $G_0W_0$ level using a spinorial Green's function. The inversion strengths introduced in the main text are computed at the $G_0W_0$ level via extrapolation to an infinite dense **k**-point mesh, by using a fitting function of the form

$$IS(N_k) = \frac{a}{N_k} + \frac{b}{\sqrt{N_k}} + c \tag{4}$$

where $N_k$ is the total number of **k**-points in the full Brillouin zone.

Part of the calculations are powered by the AiiDA[79] materials' informatics infrastructure. Direct gap metals (DGM) are identified by computing the direct band gap at every **k**-point along high-symmetry lines[47] with a **k**-point density of 0.01 Å$^{-1}$: if the system is metallic but there is a direct gap at every **k**-point, that is,

$$\min_{\mathbf{k}}(\varepsilon_{n_e+1}(\mathbf{k}) - \varepsilon_{n_e}(\mathbf{k})) > 0.01 \text{ eV} \tag{5}$$

where $n_e$ is the number of electrons (equal to the number of occupied bands in fully relativistic calculations with SOC), then the system is considered a DGM. The magnetic screening is performed with collinear DFT-PBE calculations using the procedure employed in ref 21. First, we explore whether the system is prone to magnetism by taking the primitive structure and assigning to each atom a collinear random magnetization. Five random configurations are tested by computing the total energy: if at least one configuration results in a magnetic ground state with total energy lower than the one of the initial nonmagnetic state, then the configuration is further screened for magnetism otherwise it is considered non magnetic. For the former class of structures, magnetism is further tested by building supercells up to twice the original volume, exploring a range of magnetic, antiferromagnetic and ferri-magnetic configurations. Among the different configurations, the one lowest in energy is taken to be the true ground state. In the high-throughput screening for QSHIs, we first assume nonmagnetic ground states, and after, we discard QSHI candidates that are later found to have a magnetic ground state by using the aforementioned protocol.

## ■ ASSOCIATED CONTENT

### Ⓢ Supporting Information

The Supporting Information is available free of charge on the ACS Publications website at DOI: 10.1021/acs.nanolett.9b02689.

> Optimized crystal structures, electronic bands with and without SOC, phonons, HWCC evolution, binding energy, space group, band gap, inversion strength (PDF)

## ■ AUTHOR INFORMATION

### Corresponding Authors

*E-mail: antimo.marrazzo@epfl.ch.
*E-mail: nicola.marzari@epfl.ch.

### ORCID

Antimo Marrazzo: 0000-0003-2053-9962
Marco Gibertini: 0000-0003-3980-5319
Nicola Marzari: 0000-0002-9764-0199

### Notes

The authors declare no competing financial interest.

## ■ ACKNOWLEDGMENTS

This work was supported by the NCCR MARVEL of the Swiss National Science Foundation. We acknowledge PRACE for awarding us access to MARCONI hosted at CINECA, Italy and Piz Daint hosted at CSCS, Switzerland. Simulation time on Piz Daint was also provided by CSCS though the production proposal s580. M.G. acknowledges support from the Swiss National Science Foundation through the Ambizione program.

## ■ REFERENCES

(1) König, M.; Wiedmann, S.; Brüne, C.; Roth, A.; Buhmann, H.; Molenkamp, L. W.; Qi, X. L.; Zhang, S. C. Quantum Spin Hall Insulator State in HgTe Quantum Wells. *Science* **2007**, *318* (5851), 766−770.

(2) Wang, J.; Zhang, S. C. Topological states of condensed matter. *Nat. Mater.* **2017**, *16* (11), 1062−1067.

(3) Kane, C. L.; Mele, E. J. Quantum Spin Hall Effect in Graphene. *Phys. Rev. Lett.* **2005**, *95*, 226801.

(4) Kane, C. L.; Mele, E. J. $Z_2$ Topological Order and the Quantum Spin Hall Effect. *Phys. Rev. Lett.* **2005**, *95*, 146802.

(5) Bernevig, B. A.; Zhang, S. C. Quantum Spin Hall Effect. *Phys. Rev. Lett.* **2006**, *96*, 106802.

(6) Fu, L.; Kane, C. L.; Mele, E. J. Topological Insulators in Three Dimensions. *Phys. Rev. Lett.* **2007**, *98* (10), 106803.

(7) Hasan, M. Z.; Kane, C. L. Colloquium: Topological insulators. *Rev. Mod. Phys.* **2010**, *82*, 3045.

(8) Tang, S.; Zhang, C.; Wong, D.; Pedramrazi, Z.; Tsai, H. Z.; Jia, C.; Moritz, B.; Claassen, M.; Ryu, H.; Kahn, S.; Jiang, J.; Yan, H.; Hashimoto, M.; Lu, D.; Moore, R. G.; Hwang, C. C.; Hwang, C.; Hussain, Z.; Chen, Y.; Ugeda, M. M.; Liu, Z.; Xie, X.; Devereaux, T. P.; Crommie, M. F.; Mo, S. K.; Shen, Z. X. Quantum spin Hall state in monolayer 1T′-WTe2. *Nat. Phys.* **2017**, *13* (7), 683−687.

(9) Fei, Z.; Palomaki, T.; Wu, S.; Zhao, W.; Cai, Z.; Sun, B.; Nguyen, P.; Finney, J.; Xu, X.; Cobden, D. H. Edge conduction in monolayer $WTe_2$. *Nat. Phys.* **2017**, *13* (7), 677−682.

(10) Wu, S.; Fatemi, V.; Gibson, Q. D.; Watanabe, K.; Taniguchi, T.; Cava, R. J.; Jarillo-Herrero, P. Observation of the quantum spin Hall effect up to 100 K in a monolayer crystal. *Science* **2018**, *359* (6371), 76−79.

(11) Reis, F.; Li, G.; Dudy, L.; Bauernfeind, M.; Glass, S.; Hanke, W.; Thomale, R.; Schäfer, J.; Claessen, R. Bismuthene on a SiC substrate: A candidate for a high-temperature quantum spin Hall material. *Science* **2017**, *357* (6348), 287−290.

(12) Teshome, T.; Datta, A. Topological Insulator in Two-Dimensional SiGe Induced by Biaxial Tensile Strain. *ACS Omega* **2018**, *3* (1), 1−7.

(13) Xu, Y.; Yan, B.; Zhang, H.-J.; Wang, J.; Xu, G.; Tang, P.; Duan, W.; Zhang, S.-C. Large-Gap Quantum Spin Hall Insulators in Tin Films. *Phys. Rev. Lett.* **2013**, *111*, 136804.

(14) Wang, A.; Du, A.; Zhao, M. Prediction of a large-gap quantum-spin-Hall insulator: Diamond-like GaBi bilayer. *Nano Res.* **2015**, *8* (12), 3823−3829.

(15) Geim, A.; Grigorieva, I. Van der Waals heterostructures. *Nature* **2013**, *499*, 419−425.

(16) Butler, S. Z.; Hollen, S. M.; Cao, L.; Cui, Y.; Gupta, J. A.; Gutiérrez, H. R.; Heinz, T. F.; Hong, S. S.; Huang, J.; Ismach, A. F.; Johnston-Halperin, E.; Kuno, M.; Plashnitsa, V. V.; Robinson, R. D.; Ruoff, R. S.; Salahuddin, S.; Shan, J.; Shi, L.; Spencer, M. G.; Terrones, M.; Windl, W.; Goldberger, J. E. Progress, challenges, and opportunities in two-dimensional materials beyond graphene. *ACS Nano* **2013**, *7*, 2898−2926.

(17) Bernevig, B. A.; Hughes, T. L. *Topological Insulators and Topological Superconductors*; Princeton University Press, 2013.

(18) Qian, X.; Liu, J.; Fu, L.; Li, J. Quantum spin Hall effect in two-dimensional transition metal dichalcogenides. *Science* **2014**, *346* (6215), 1344−1347.

(19) Antonius, G.; Louie, S. G. Temperature-Induced Topological Phase Transitions: Promoted versus Suppressed Nontrivial Topology. *Phys. Rev. Lett.* **2016**, *117* (24), 246401.

(20) Monserrat, B.; Vanderbilt, D. Temperature Effects in the Band Structure of Topological Insulators. *Phys. Rev. Lett.* **2016**, *117* (22), 226801.

(21) Mounet, N.; Gibertini, M.; Schwaller, P.; Campi, D.; Merkys, A.; Marrazzo, A.; Sohier, T.; Castelli, I. E.; Cepellotti, A.; Pizzi, G.; Marzari, N. Two-dimensional materials from high-throughput computational exfoliation of experimentally known compounds. *Nat. Nanotechnol.* **2018**, *13* (3), 246−252.

(22) Haastrup, S.; Strange, M.; Pandey, M.; Deilmann, T.; Schmidt, P. S.; Hinsche, N. F.; Gjerding, M. N.; Torelli, D.; Larsen, P. M.; Riis-Jensen, A. C.; Gath, J.; Jacobsen, K. W.; Mortensen, J. J.; Olsen, T.; Thygesen, K. S. The Computational 2D Materials Database: high-throughput modeling and discovery of atomically thin crystals. *2D Mater.* **2018**, *5* (4), 042002.

(23) Olsen, T.; Andersen, E.; Okugawa, T.; Torelli, D.; Deilmann, T.; Thygesen, K. S. Discovering two-dimensional topological insulators from high-throughput computations. *Phys. Rev. Mater.* **2019**, *3* (2), 024005.

(24) Yang, K.; Setyawan, W.; Wang, S.; Nardelli, M. B.; Curtarolo, S. A search model for topological insulators with high-throughput robustness descriptors. *Nat. Mater.* **2012**, *11* (7), 614–619.

(25) Choudhary, K.; Garrity, K. F.; Tavazza, F. High-throughput discovery of topological materials using spin-orbit spillage. *Sci. Rep.* **2019**, *9*, 8534.

(26) For 165 compounds, standard nonmagnetic structural optimization did not succeed, mostly due either to the presence of magnetic elements or to unstable structures.

(27) We further screen out compounds with band inversions (see later in the text) smaller than 20 meV.

(28) Sgiarovello, C.; Peressi, M.; Resta, R. Electron localization in the insulating state: Application to crystalline semiconductors. *Phys. Rev. B: Condens. Matter Mater. Phys.* **2001**, *64* (11), 115202.

(29) Soluyanov, A. A.; Vanderbilt, D. Computing topological invariants without inversion symmetry. *Phys. Rev. B: Condens. Matter Mater. Phys.* **2011**, *83* (23), 235401.

(30) Gresch, D.; Autès, G.; Yazyev, O. V.; Troyer, M.; Vanderbilt, D.; Bernevig, B. A.; Soluyanov, A. A. Z2Pack: Numerical implementation of hybrid Wannier centers for identifying topological materials. *Phys. Rev. B: Condens. Matter Mater. Phys.* **2017**, *95* (7), 075146.

(31) Baroni, S.; de Gironcoli, S.; Dal Corso, A.; Giannozzi, P. Phonons and related crystal properties from density-functional perturbation theory. *Rev. Mod. Phys.* **2001**, *73* (2), 515–562.

(32) Liu, J.; Vanderbilt, D. Spin-orbit spillage as a measure of band inversion in insulators. *Phys. Rev. B: Condens. Matter Mater. Phys.* **2014**, *90* (12), 125133.

(33) Slager, R.-J.; Mesaros, A.; Juricic, V.; Zaanen, J. The space group classification of topological band-insulators. *Nat. Phys.* **2013**, *9*, 98–102.

(34) Kruthoff, J.; de Boer, J.; van Wezel, J.; Kane, C. L.; Slager, R. J. Topological Classification of Crystalline Insulators through Band Structure Combinatorics. *Phys. Rev. X* **2017**, *7*, 041069.

(35) Bradlyn, B.; Elcoro, L.; Cano, J.; Vergniory, M. G.; Wang, Z.; Felser, C.; Aroyo, M. I.; Bernevig, B. A. Topological quantum chemistry. *Nature* **2017**, *547* (7663), 298–305.

(36) Vergniory, M. G.; Elcoro, L.; Felser, C.; Regnault, N.; Bernevig, B. A.; Wang, Z. A complete catalogue of high-quality topological materials. *Nature* **2019**, *566* (7745), 480.

(37) Tang, F.; Po, H. C.; Vishwanath, A.; Wan, X. Comprehensive search for topological materials using symmetry indicators. *Nature* **2019**, *566* (7745), 486.

(38) Zhang, T.; Jiang, Y.; Song, Z.; Huang, H.; He, Y.; Fang, Z.; Weng, H.; Fang, C. Catalogue of topological electronic materials. *Nature* **2019**, *566* (7745), 475.

(39) Zunger, A. Beware of plausible predictions of fantasy materials. *Nature* **2019**, *566* (7745), 447.

(40) von Klitzing, K. The quantized Hall effect. *Rev. Mod. Phys.* **1986**, *58* (3), 519–531.

(41) Vidal, J.; Zhang, X.; Yu, L.; Luo, J. W.; Zunger, A. False-positive and false-negative assignments of topological insulators in density functional theory and hybrids. *Phys. Rev. B: Condens. Matter Mater. Phys.* **2011**, *84* (4), 041109.

(42) Autès, G.; Isaeva, A.; Moreschini, L.; Johannsen, J. C.; Pisoni, A.; Mori, R.; Zhang, W.; Filatova, T. G.; Kuznetsov, A. N.; Forró, L.; Van den Broek, W.; Kim, Y.; Kim, K. S.; Lanzara, A.; Denlinger, J. D.; Rotenberg, E.; Bostwick, A.; Grioni, M.; Yazyev, O. V. A novel quasi-one-dimensional topological insulator in bismuth iodide $\beta$-Bi$_4$I$_4$. *Nat. Mater.* **2016**, *15* (2), 154–158.

(43) Marrazzo, A.; Gibertini, M.; Campi, D.; Mounet, N.; Marzari, N. Prediction of a Large-Gap and Switchable Kane-Mele Quantum Spin Hall Insulator. *Phys. Rev. Lett.* **2018**, *120* (11), 117701.

(44) Molle, A.; Goldberger, J.; Houssa, M.; Xu, Y.; Zhang, S. C.; Akinwande, D. Buckled two-dimensional Xene sheets. *Nat. Mater.* **2017**, *16* (2), 163–169.

(45) Liu, J.; Wang, H.; Fang, C.; Fu, L.; Qian, X. Van der Waals Stacking-Induced Topological Phase Transition in Layered Ternary Transition Metal Chalcogenides. *Nano Lett.* **2017**, *17* (1), 467–475.

(46) Monserrat, B.; Vanderbilt, D. Phonon-assisted spin splitting in centrosymmetric crystals. *arXiv:1711.06274 [cond-mat]* **2017**.

(47) Ramíarez, R.; Böhm, M. C. Simple geometric generation of special points in brillouin-zone integrations. Two-dimensional bravais lattices. *Int. J. Quantum Chem.* **1986**, *30* (3), 391–411.

(48) Bernevig, B. A.; Hughes, T. L.; Zhang, S. C. Quantum Spin Hall Effect and Topological Phase Transition in HgTe Quantum Wells. *Science* **2006**, *314* (5806), 1757–1761.

(49) Hüser, F.; Olsen, T.; Thygesen, K. S. How dielectric screening in two-dimensional crystals affects the convergence of excited-state calculations: Monolayer MoS$_2$. *Phys. Rev. B: Condens. Matter Mater. Phys.* **2013**, *88* (24), 245309.

(50) Rasmussen, F. A.; Schmidt, P. S.; Winther, K. T.; Thygesen, K. S. Efficient many-body calculations for two-dimensional materials using exact limits for the screened potential: Band gaps of MoS$_2$,h-BN, and phosphorene. *Phys. Rev. B: Condens. Matter Mater. Phys.* **2016**, *94* (15), 155406.

(51) Wang, A.; Wang, A.; Du, A.; Zhao, M. Band inversion and topological aspects in a TiNI monolayer. *Phys. Chem. Chem. Phys.* **2016**, *18* (32), 22154–22159.

(52) Li, X.; Zhang, Z.; Yao, Y.; Zhang, H. High throughput screening for two-dimensional topological insulators. *2D Mater.* **2018**, *5* (4), 045023.

(53) Zhou, L.; Kou, L.; Sun, Y.; Felser, C.; Hu, F.; Shan, G.; Smith, S. C.; Yan, B.; Frauenheim, T. New Family of Quantum Spin Hall Insulators in Two-dimensional Transition-Metal Halide with Large Nontrivial Band Gaps. *Nano Lett.* **2015**, *12* (15), 7867–7872.

(54) Laufek, F.; Vymazalová, A.; Drábek, M. Powder diffraction study of Pd$_2$HgSe$_3$. *Powder Diffr.* **2017**, *32* (4), 244–248.

(55) Drábek, M.; Vymazalová, A.; Laufek, F. The system Hg–Pd–Se at 400 °C: phase relations involving tischendorgite and other ternary phases. *Can. Mineral.* **2014**, *52* (4), 763–768.

(56) Murakami, S. Quantum Spin Hall Effect and Enhanced Magnetic Response by Spin-Orbit Coupling. *Phys. Rev. Lett.* **2006**, *97* (23), 236805.

(57) Drozdov, I. K.; Alexandradinata, A.; Jeon, S.; Nadj-Perge, S.; Ji, H.; Cava, R. J.; Bernevig, B. A.; Yazdani, A. One-dimensional topological edge states of bismuth bilayers. *Nat. Phys.* **2014**, *10* (9), 664–669.

(58) Peng, L.; Xian, J. J.; Tang, P.; Rubio, A.; Zhang, S. C.; Zhang, W.; Fu, Y. S. Visualizing topological edge states of single and double bilayer Bi supported on multibilayer Bi(111) films. *Phys. Rev. B: Condens. Matter Mater. Phys.* **2018**, *98* (24), 245108.

(59) Sabater, C.; Gosálbez-Martínez, D.; Fernández-Rossier, J.; Rodrigo, J. G.; Untiedt, C.; Palacios, J. J. Topologically Protected Quantum Transport in Locally Exfoliated Bismuth at Room Temperature. *Phys. Rev. Lett.* **2013**, *110*, 176802.

(60) Xiang, H.; Xu, B.; Liu, J.; Xia, Y.; Lu, H.; Yin, J.; Liu, Z. Quantum spin Hall insulator phase in monolayer WTe$_2$ by uniaxial strain. *AIP Adv.* **2016**, *6* (9), 095005.

(61) Zheng, F.; Cai, C.; Ge, S.; Zhang, X.; Liu, X.; Lu, H.; Zhang, Y.; Qiu, J.; Taniguchi, T.; Watanabe, K.; Jia, S.; Qi, J.; Chen, J. H.; Sun, D.; Feng, J. On the Quantum Spin Hall Gap of Monolayer 1T′-WTe$_2$. *Adv. Mater.* **2016**, *28* (24), 4845–4851.

(62) Lee, K.; Murray, É. D.; Kong, L.; Lundqvist, B. I.; Langreth, D. C. Higher-accuracy van der Waals density functional. *Phys. Rev. B: Condens. Matter Mater. Phys.* **2010**, *82* (8), 081101.

(63) Cooper, V. R. Van der Waals density functional: An appropriate exchange functional. *Phys. Rev. B: Condens. Matter Mater. Phys.* **2010**, *81* (16), 161104.

(64) Giannozzi, P.; Baroni, S.; Bonini, N.; Calandra, M.; Car, R.; Cavazzoni, C.; Ceresoli, D.; Chiarotti, G. L.; Cococcioni, M.; Dabo, I.; Dal Corso, A.; de Gironcoli, S.; Fabris, S.; Fratesi, G.; Gebauer, R.; Gerstmann, U.; Gougoussis, C.; Kokalj, A.; Lazzeri, M.; Martin-Samos, L.; Marzari, N.; Mauri, F.; Mazzarello, R.; Paolini, S.; Pasquarello, A.; Paulatto, L.; Sbraccia, C.; Scandolo, S.; Sclauzero, G.; Seitsonen, A. P.; Smogunov, A.; Umari, P.; Wentzcovitch, R. M. QUANTUM ESPRESSO: A modular and open-source software

project for quantum simulations of materials. *J. Phys.: Condens. Matter* **2009**, *21* (39), 395502.

(65) Giannozzi, P.; Andreussi, O.; Brumme, T.; Bunau, O.; Nardelli, M. B.; Calandra, M.; Car, R.; Cavazzoni, C.; Ceresoli, D.; Cococcioni, M.; Colonna, N.; Carnimeo, I.; Dal Corso, A.; de Gironcoli, S.; Delugas, P.; DiStasio, R. A., Jr; Ferretti, A.; Floris, A.; Fratesi, G.; Fugallo, G.; Gebauer, R.; Gerstmann, U.; Giustino, F.; Gorni, T.; Jia, J.; Kawamura, M.; Ko, H.-Y.; Kokalj, A.; Küçükbenli, E.; Lazzeri, M.; Marsili, M.; Marzari, N.; Mauri, F.; Nguyen, N. L.; Nguyen, H. V.; Otero de la Roza, A.; Paulatto, L.; Poncé, S.; Rocca, D.; Sabatini, R.; Santra, B.; Schlipf, M.; Seitsonen, A. P.; Smogunov, A.; Timrov, I.; Thonhauser, T.; Umari, P.; Vast, N.; Wu, X.; Baroni, S. Advanced capabilities for materials modelling with Quantum ESPRESSO. *J. Phys.: Condens. Matter* **2017**, *29* (46), 465901.

(66) Prandini, G.; Marrazzo, A.; Castelli, I. E.; Mounet, N.; Marzari, N. Precision and efficiency in solid-state pseudopotential calculations. *Npj Comput. Mater.* **2018**, *4*, 72.

(67) Hamann, D. R. Optimized norm-conserving Vanderbilt pseudopotentials. *Phys. Rev. B: Condens. Matter Mater. Phys.* **2013**, *88* (8), 085117.

(68) van Setten, M. J.; Giantomassi, M.; Bousquet, E.; Verstraete, M. J.; Hamann, D. R.; Gonze, X.; Rignanese, G. M. The PseudoDojo: Training and grading a 85 element optimized norm-conserving pseudopotential table. *Comput. Phys. Commun.* **2018**, *226*, 39−54.

(69) Lejaeghere, K.; Bihlmayer, G.; Björkman, T.; Blaha, P.; Blügel, S.; Blum, V.; Caliste, D.; Castelli, I. E.; Clark, S. J.; Dal Corso, A.; de Gironcoli, S.; Deutsch; Dewhurst, J. K.; Di Marco, I.; Draxl, C.; Dułak, M.; Eriksson, O.; Flores-Livas, J. A.; Garrity, K. F.; Genovese, L.; Giannozzi, P.; Giantomassi, M.; Goedecker, S.; Gonze, X.; Grånäs, O.; Gross, E. K. U.; Gulans, A.; Gygi, F.; Hamann, D. R.; Hasnip, P. J.; Holzwarth, N. a. W.; Luşan, D.; Jochym, D. B.; Jollet, F.; Jones, D.; Kresse, G.; Koepernik, K.; Küçükbenli, E.; Kvashnin, Y. O.; Locht, I. L. M.; Lubeck, S.; Marsman, M.; Marzari, N.; Nitzsche, U.; Nordström, L.; Ozaki, T.; Paulatto, L.; Pickard, C. J.; Poelmans, W.; Probert, M. I. J.; Refson, K.; Richter, M.; Rignanese, G. M.; Saha, S.; Scheffler, M.; Schlipf, M.; Schwarz, K.; Sharma, S.; Tavazza, F.; Thunström, P.; Tkatchenko, A.; Torrent, M.; Vanderbilt, D.; van Setten, M. J.; Van Speybroeck, V.; Wills, J. M.; Yates, J. R.; Zhang, G. X.; Cottenier, S. Reproducibility in density functional theory calculations of solids. *Science* **2016**, *351* (6280), aad3000.

(70) Marzari, N.; Vanderbilt, D.; De Vita, A.; Payne, M. C. Thermal Contraction and Disordering of the Al(110) Surface. *Phys. Rev. Lett.* **1999**, *82* (16), 3296−3299.

(71) Vydrov, O. A.; Van Voorhis, T. Nonlocal van der Waals Density Functional Made Simple. *Phys. Rev. Lett.* **2009**, *103* (6), 063004.

(72) Sabatini, R.; Gorni, T.; de Gironcoli, S. Nonlocal van der Waals density functional made simple and efficient. *Phys. Rev. B: Condens. Matter Mater. Phys.* **2013**, *87* (4), 041108.

(73) Sohier, T.; Calandra, M.; Mauri, F. Density functional perturbation theory for gated two-dimensional heterostructures: Theoretical developments and application to flexural phonons in graphene. *Phys. Rev. B: Condens. Matter Mater. Phys.* **2017**, *96*, 075448.

(74) Sohier, T.; Gibertini, M.; Calandra, M.; Mauri, F.; Marzari, N. Breakdown of Optical Phonons' Splitting in Two-Dimensional Materials. *Nano Lett.* **2017**, *17* (6), 3758−3763.

(75) Marini, A.; Hogan, C.; Grüning, M.; Varsano, D. yambo: An ab initio tool for excited state calculations. *Comput. Phys. Commun.* **2009**, *180* (8), 1392−1403.

(76) Sangalli, D.; Ferretti, A.; Miranda, H.; Attaccalite, C.; Marri, I.; Cannuccia, E.; Melo, P.; Marsili, M.; Paleari, F.; Marrazzo, A.; Prandini, G.; Bonfà, P.; Atambo, M. O.; Affinito, F.; Palummo, M.; Molina-Sánchez, A.; Hogan, C.; Grüning, M.; Varsano, D.; Marini, A. Many-body perturbation theory calculations using the yambo code. *J. Phys.: Condens. Matter* **2019**, *31*, 32.

(77) Godby, R. W.; Needs, R. J. Metal-insulator transition in Kohn-Sham theory and quasiparticle theory. *Phys. Rev. Lett.* **1989**, *62* (10), 1169−1172.

(78) Oschlies, A.; Godby, R. W.; Needs, R. J. GW self-energy calculations of carrier-induced band-gap narrowing in n-type silicon. *Phys. Rev. B: Condens. Matter Mater. Phys.* **1995**, *51* (3), 1527−1535.

(79) Pizzi, G.; Cepellotti, A.; Sabatini, R.; Marzari, N.; Kozinsky, B. AiiDA: Automated interactive infrastructure and database for computational science. *Comput. Mater. Sci.* **2016**, *111*, 218−230.

# Supporting Information for
# Relative Abundance of $\mathbb{Z}_2$ Topological Order in Exfoliable Two-dimensional Insulators

Antimo Marrazzo,[1] Marco Gibertini,[1,2] Davide Campi,[1] Nicolas Mounet,[1] and Nicola Marzari[1]

[1] *Theory and Simulation of Materials (THEOS) and National Centre for Computational Design and Discovery of Novel Materials (MARVEL), École Polytechnique Fédérale de Lausanne, 1015, Switzerland*

[2] *Department of Quantum Matter Physics, University of Geneva,*
*24 Quai Ernest Ansermet, CH-1211 Geneva, Switzerland*

# 1. AsCuLi$_2$

## Info and properties

| | | | |
|---|---|---|---|
| **Formula (DB ID)** | AsCuLi$_2$ (ICSD 153858) | **No. atoms per unit cell** | 4 |
| **Spacegroup** | P$\bar{6}m2$ (187) | **DF2-C09 Binding energy [meV/Å$^2$]** | 63 |
| **DFT band gap [meV]** | 45 | **rVV10 Binding energy [meV/Å$^2$]** | 62 |
| **DFT inversion strength [meV]** | 80 | **G$_0$W$_0$ inversion strength [meV]** | 169 |

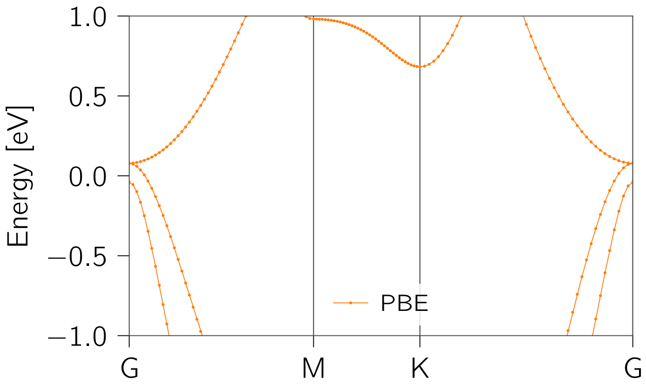

**Figure S1.1** DFT band structure

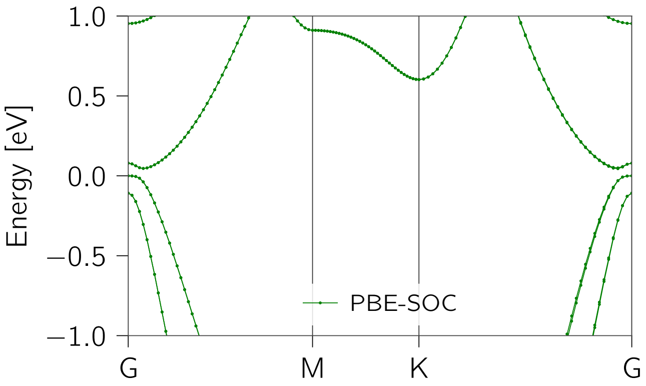

**Figure S1.2** DFT band structure with spin-orbit coupling

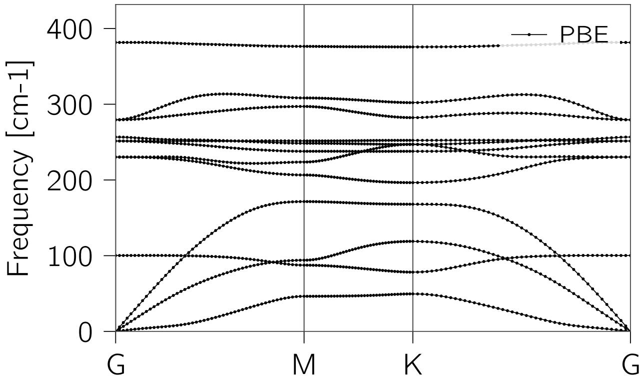

**Figure S1.3** DFPT phonons dispersions

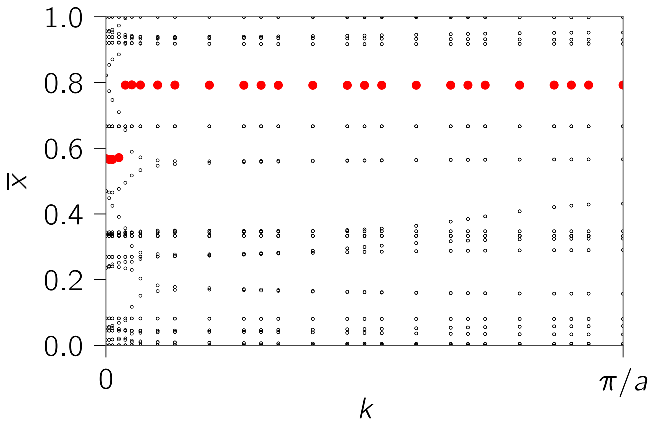

**Figure S1.4** HWCC evolution (empty circles) together with their largest gap (full, red circles)

**Figure S1.5** Orthographic projections

Li and As atoms are purple, Cu atoms are brown.

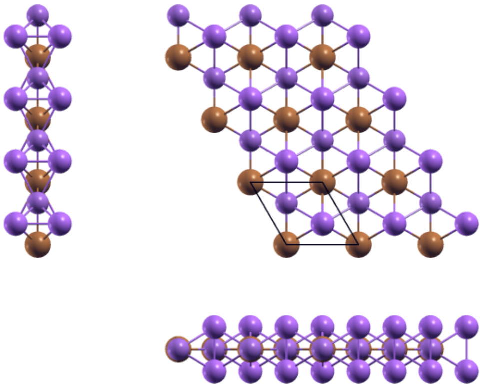

**Table S1.1** Structural parameters: relaxed cell and atomic positions in cartesian coordinates

| | $x$ [Å] | $y$ [Å] | $z$ [Å] |
|---|---|---|---|
| $\boldsymbol{a_1}$ | 4.135169 | −0.000000 | 0.000000 |
| $\boldsymbol{a_2}$ | −2.067584 | 3.581161 | 0.000000 |
| $\boldsymbol{a_3}$ | 0.000000 | 0.000000 | 22.619834 |
| ● Li | 2.067584 | 1.193720 | 12.576172 |
| ● Li | 2.067584 | 1.193720 | 10.043662 |
| ● Cu | −0.000000 | 0.000000 | 11.309917 |
| ● As | 0.000000 | 2.387441 | 11.309917 |

# 2. Bi

## Info and properties

| | | | |
|---|---|---|---|
| **Formula (DB ID)** | Bi (ICSD 43938) | **No. atoms per unit cell** | 2 |
| **Spacegroup** | P$\bar{3}m1$ (164) | **DF2-C09 Binding energy [meV/Å$^2$]** | 18 |
| **DFT band gap [meV]** | 545 | **rVV10 Binding energy [meV/Å$^2$]** | 25 |
| **DFT inversion strength [meV]** | 685 | **$G_0W_0$ inversion strength [meV]** | 760 |

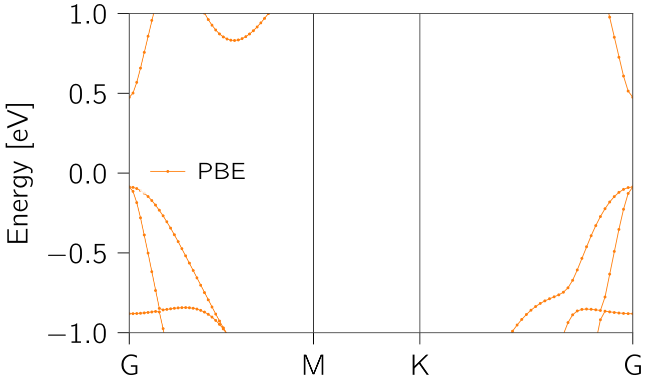

**Figure S2.1** DFT band structure

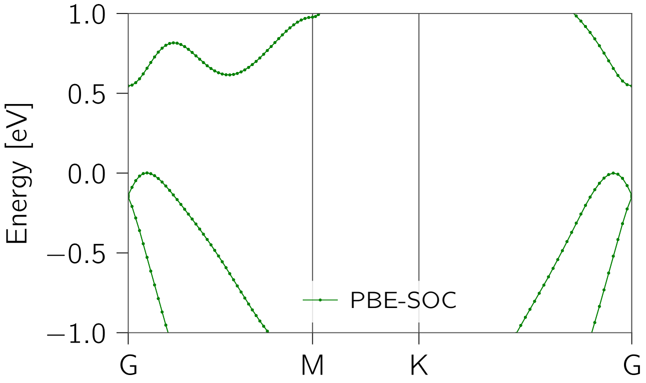

**Figure S2.2** DFT band structure with spin-orbit coupling

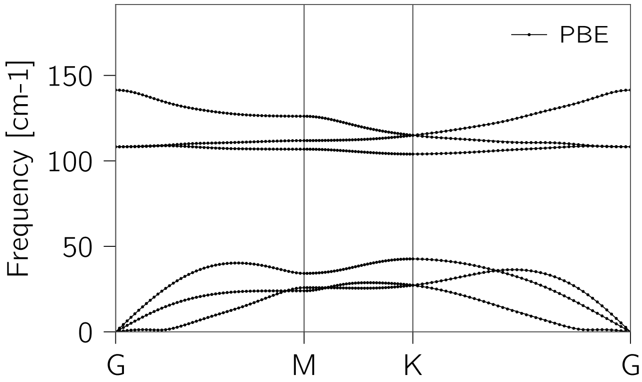

**Figure S2.3** DFPT phonons dispersions

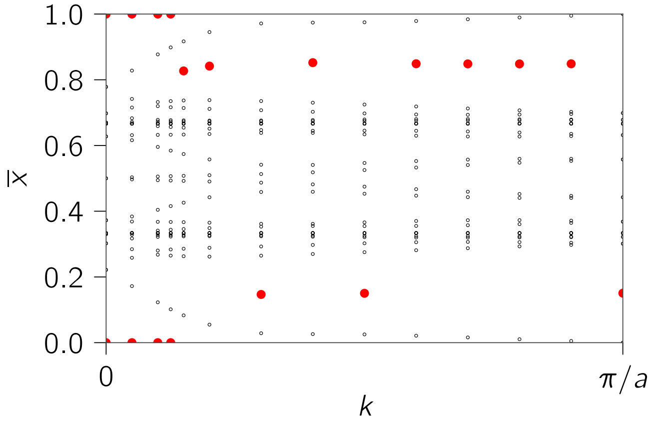

**Figure S2.4** HWCC evolution (empty circles) together with their largest gap (full, red circles)

**Figure S2.5** Orthographic projections

Bi atoms are purple.

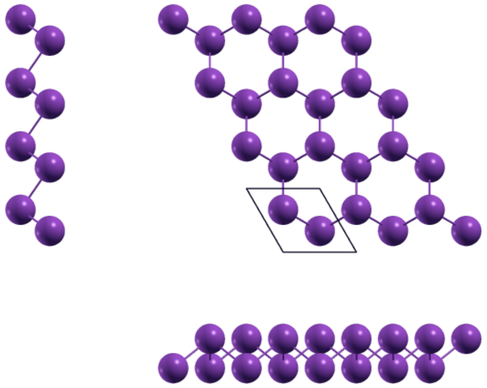

**Table S2.1** Structural parameters: relaxed cell and atomic positions in cartesian coordinates

| | $x$ [Å] | $y$ [Å] | $z$ [Å] |
|---|---|---|---|
| $\boldsymbol{a_1}$ | 4.332356 | 0.000000 | 0.000000 |
| $\boldsymbol{a_2}$ | −2.166178 | 3.751931 | 0.000000 |
| $\boldsymbol{a_3}$ | 0.000000 | 0.000000 | 21.666277 |
| ● Bi | 2.166178 | 1.250644 | 9.967806 |
| ● Bi | 0.000000 | 2.501287 | 11.698471 |

# 3. ZrBr

## Info and properties

| | |
|---|---|
| **Formula (DB ID)** | ZrBr (COD 4343762) |
| **Spacegroup** | $P2_1/m$ (11) |
| **DFT band gap [meV]** | 29 (at 1 % strain) |
| **DFT inversion strength [meV]** | 45 (at 1 % strain) |

| | |
|---|---|
| **No. atoms per unit cell** | 4 |
| **DF2-C09 Binding energy [meV/Å$^2$]** | 16 |
| **rVV10 Binding energy [meV/Å$^2$]** | 22 |

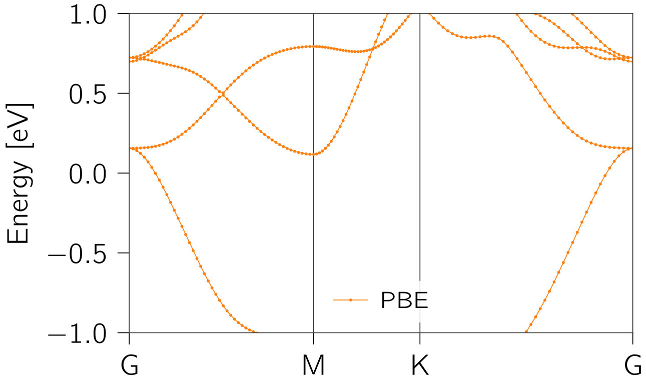

**Figure S3.1** DFT band structure

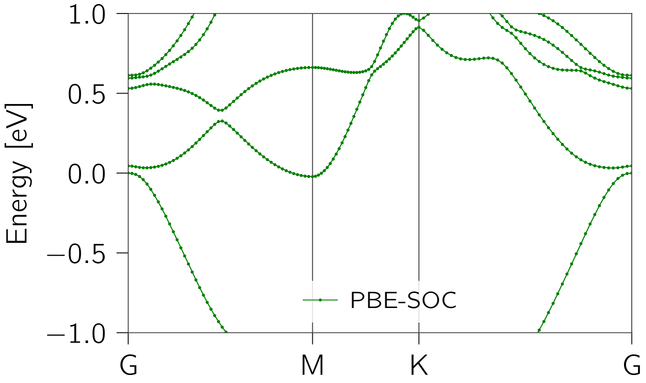

**Figure S3.2** DFT band structure with spin-orbit coupling

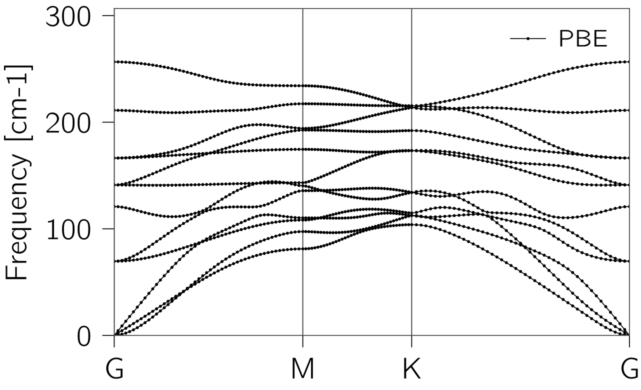

**Figure S3.3** DFPT phonons dispersions

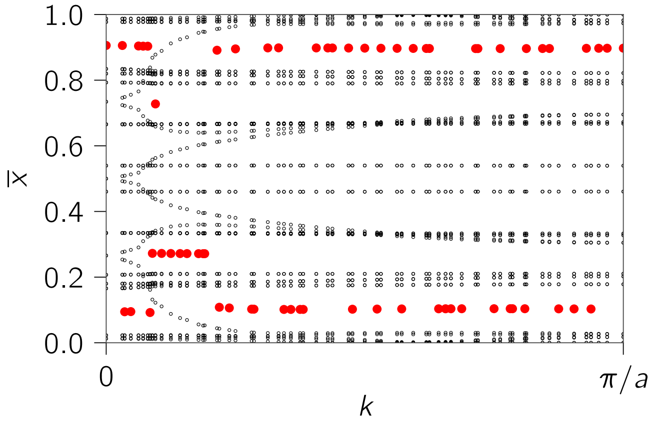

**Figure S3.4** HWCC evolution (empty circles) together with their largest gap (full, red circles)

**Figure S3.5** Orthographic projections

Br atoms are red, Zr atoms are light blue.

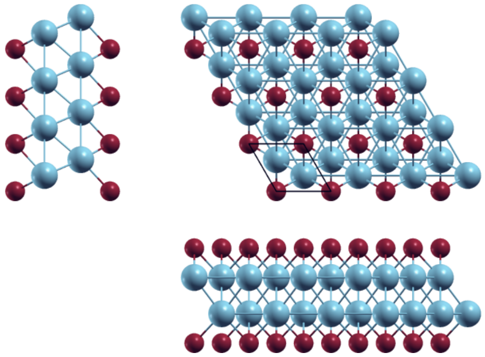

**Table S3.1** Structural parameters: relaxed cell and atomic positions in cartesian coordinates

| | $x$ [Å] | $y$ [Å] | $z$ [Å] |
|---|---|---|---|
| $\boldsymbol{a}_1$ | 3.533584 | −0.000000 | 0.000000 |
| $\boldsymbol{a}_2$ | −1.766792 | 3.060173 | 0.000000 |
| $\boldsymbol{a}_3$ | 0.000000 | 0.000000 | 26.190223 |
| 🔵 Zr | −0.000000 | 2.040115 | 11.922714 |
| 🔴 Br | 0.000000 | 0.000000 | 10.030397 |
| 🔴 Br | −0.000000 | −0.000000 | 16.159826 |
| 🔵 Zr | 1.766792 | 1.020058 | 14.267509 |

# 4. ZrCl

## Info and properties

| | |
|---|---|
| **Formula (DB ID)** | ZrCl (ICSD 20148) |
| **Spacegroup** | $P2_1/m$ (11) |
| **DFT band gap [meV]** | 39 (at 3 % strain) |
| **DFT inversion strength [meV]** | 60 (at 3 % strain) |
| **No. atoms per unit cell** | 4 |
| **DF2-C09 Binding energy [meV/Å$^2$]** | 15 |
| **rVV10 Binding energy [meV/Å$^2$]** | 22 |

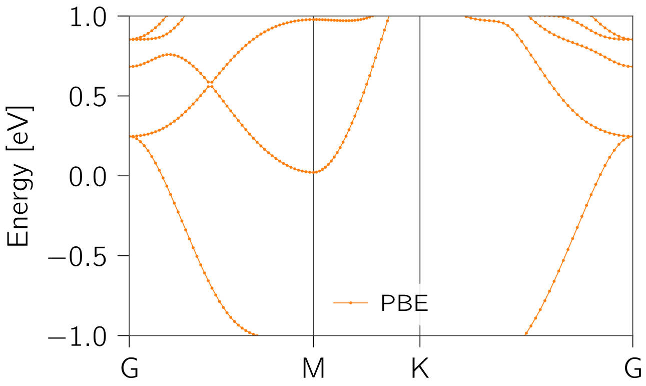

**Figure S4.1** DFT band structure

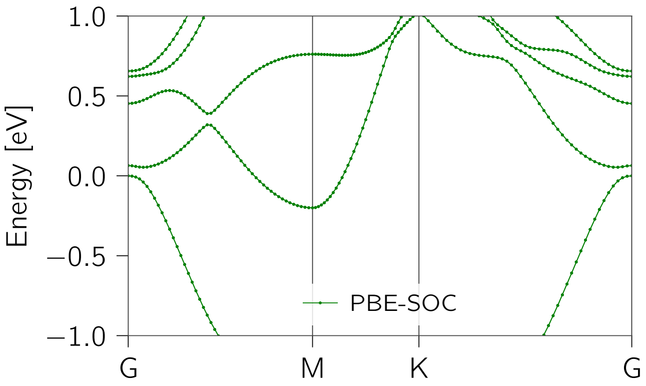

**Figure S4.2** DFT band structure with spin-orbit coupling

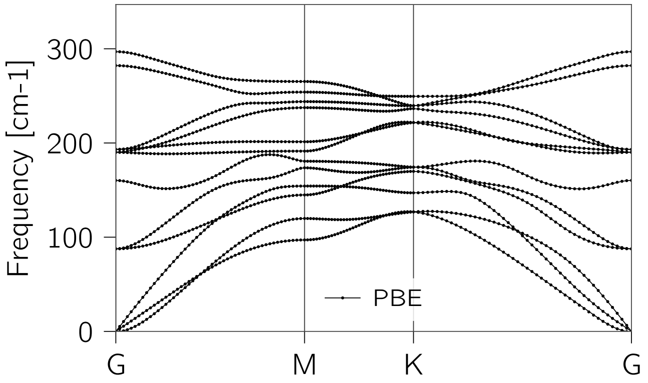

**Figure S4.3** DFPT phonons dispersions

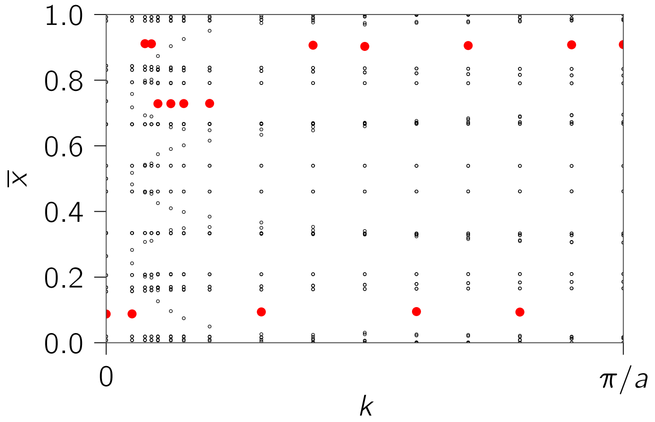

**Figure S4.4** HWCC evolution (empty circles) together with their largest gap (full, red circles)

**Figure S4.5** Orthographic projections

Cl atoms are green, Zr atoms are light blue.

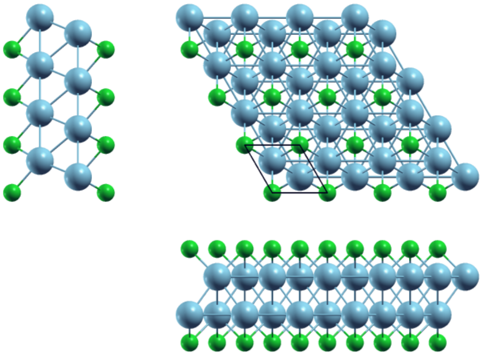

**Table S4.1** Structural parameters: relaxed cell and atomic positions in cartesian coordinates

| | $x$ [Å] | $y$ [Å] | $z$ [Å] |
|---|---:|---:|---:|
| $\boldsymbol{a_1}$ | 3.445821 | 0.000000 | 0.000000 |
| $\boldsymbol{a_2}$ | −1.722910 | 2.984168 | 0.000000 |
| $\boldsymbol{a_3}$ | 0.000000 | 0.000000 | 25.910261 |
| ● Zr | 1.722910 | 0.994723 | 11.765738 |
| ● Cl | 0.000000 | −0.000000 | 15.884383 |
| ● Cl | 0.000000 | −0.000000 | 10.025878 |
| ● Zr | 0.000000 | 1.989446 | 14.144523 |

# 5. $TiCu_2Te_3$

## Info and properties

| | | | |
|---|---|---|---|
| **Formula (DB ID)** | $TiCu_2Te_3$ (ICSD 402631) | **No. atoms per unit cell** | 12 |
| **Spacegroup** | C2/$m$ (2) | **DF2-C09 Binding energy [meV/Å$^2$]** | 44 |
| **DFT band gap [meV]** | 8 | **rVV10 Binding energy [meV/Å$^2$]** | 44 |
| **DFT inversion strength [meV]** | 21 | | |

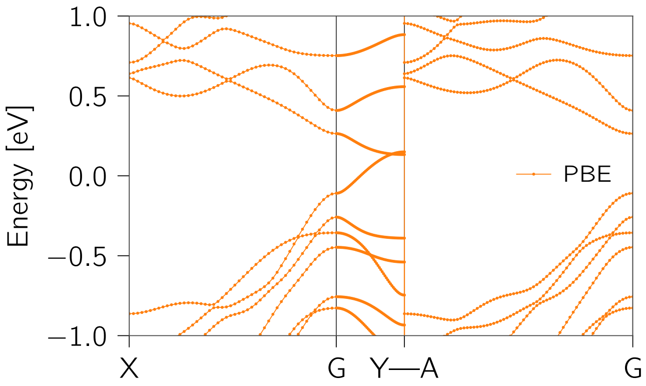

**Figure S5.1** DFT band structure

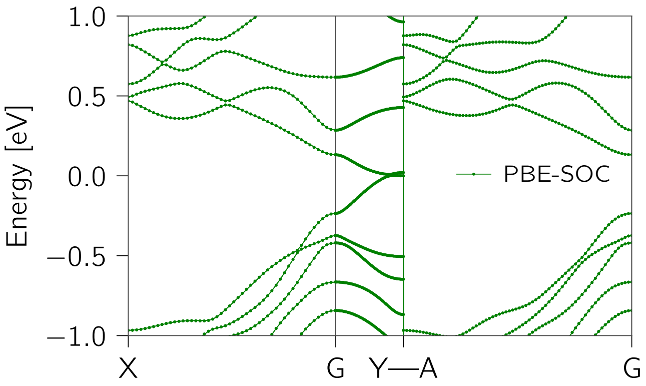

**Figure S5.2** DFT band structure with spin-orbit coupling

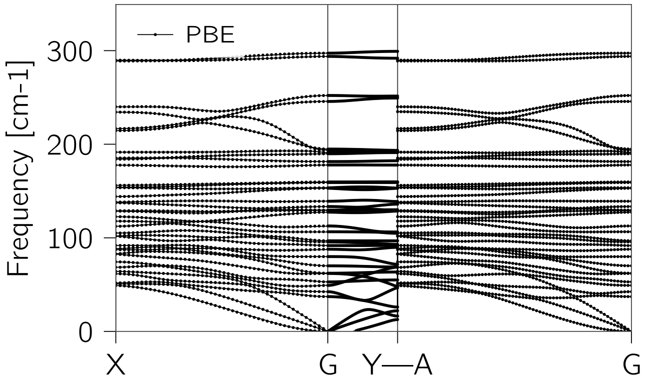

**Figure S5.3** DFPT phonons dispersions

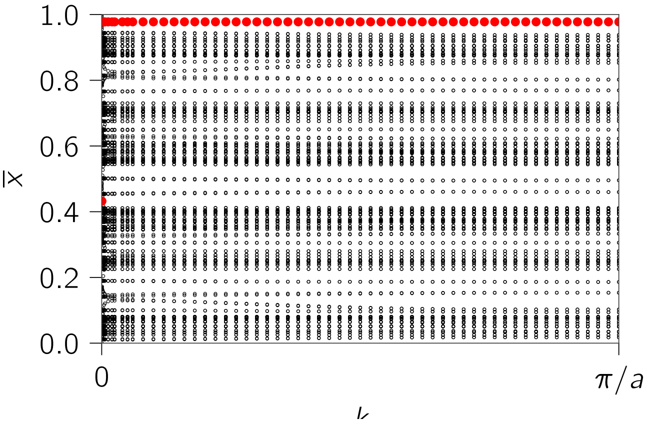

**Figure S5.4** HWCC evolution (empty circles) together with their largest gap (full, red circles)

**Figure S5.5** Orthographic projections

Ti atoms are grey, Cu and Te atoms are brown.

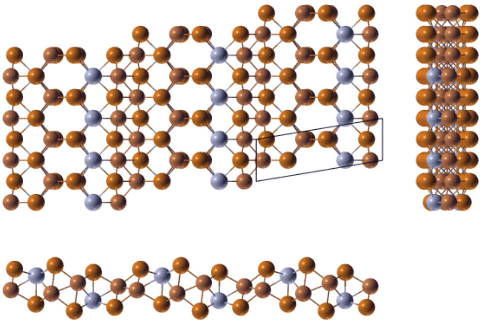

**Table S5.1** Structural parameters: relaxed cell and atomic positions in cartesian coordinates

| | $x$ [Å] | $y$ [Å] | $z$ [Å] |
|---|---|---|---|
| $\boldsymbol{a_1}$ | 3.889296 | 0.000001 | 0.000000 |
| $\boldsymbol{a_2}$ | −1.944646 | 11.657059 | 0.000000 |
| $\boldsymbol{a_3}$ | 0.000000 | 0.000000 | 24.320763 |
| ● Cu | 1.944623 | 4.862542 | 11.663966 |
| ● Te | 1.944654 | 1.455332 | 13.926122 |
| ● Te | 1.944660 | 5.194468 | 14.267237 |
| ● Ti | 0.000016 | 8.712668 | 11.009569 |
| ● Ti | 0.000009 | 3.463583 | 13.311190 |
| ● Cu | −0.000023 | 11.062781 | 12.334616 |
| ● Cu | −0.000013 | 1.113422 | 11.986169 |
| ● Te | 0.000011 | 8.754268 | 13.634626 |
| ● Te | −0.000014 | 3.421968 | 10.686139 |
| ● Cu | 1.944653 | 7.313692 | 12.656787 |
| ● Te | 1.944657 | 10.720921 | 10.394636 |
| ● Te | 1.944666 | 6.981789 | 10.053522 |

# 6. TiNI

## Info and properties

| | | | |
|---|---|---|---|
| **Formula (DB ID)** | TiNI (ICSD 27394) | **No. atoms per unit cell** | 6 |
| **Spacegroup** | P$mmn$(59) | **DF2-C09 Binding energy [meV/Å$^2$]** | 15 |
| **DFT band gap [meV]** | 18 | **rVV10 Binding energy [meV/Å$^2$]** | 22 |
| **DFT inversion strength [meV]** | 141 | **$G_0W_0$ inversion strength [meV]** | -705 (trivial) |

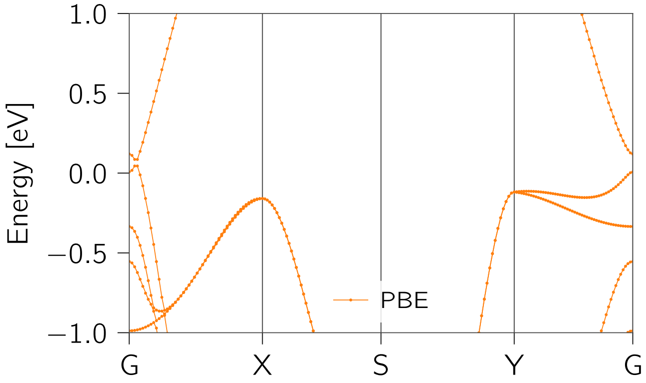

**Figure S6.1** DFT band structure

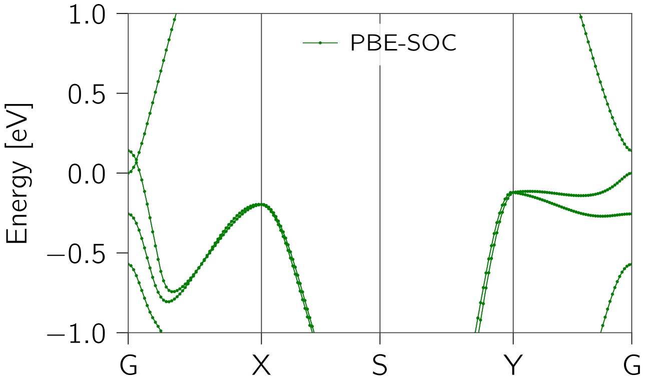

**Figure S6.2** DFT band structure with spin-orbit coupling

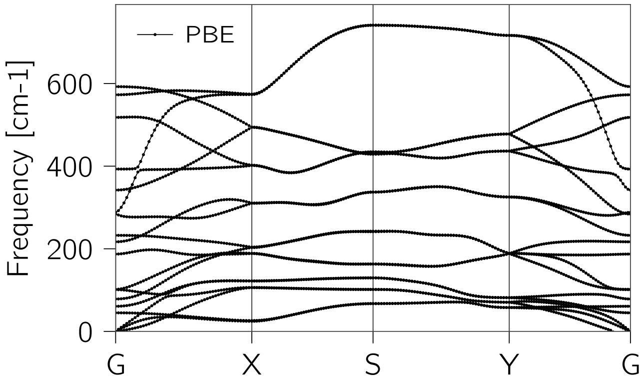

**Figure S6.3** DFPT phonons dispersions

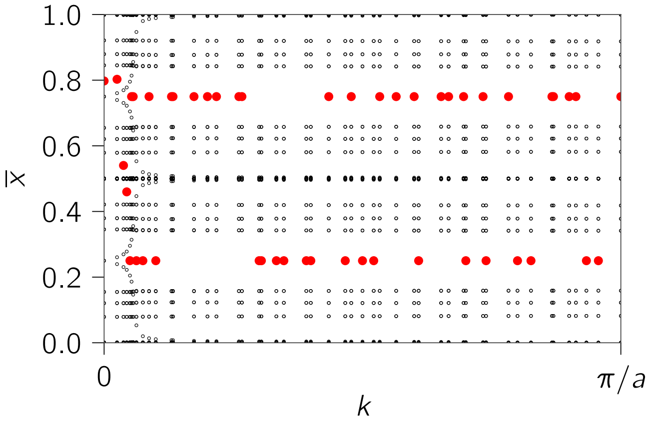

**Figure S6.4** HWCC evolution (empty circles) together with their largest gap (full, red circles)

**Figure S6.5** Orthographic projections

N atoms are blue, Ti atoms are grey, I atoms are purple.

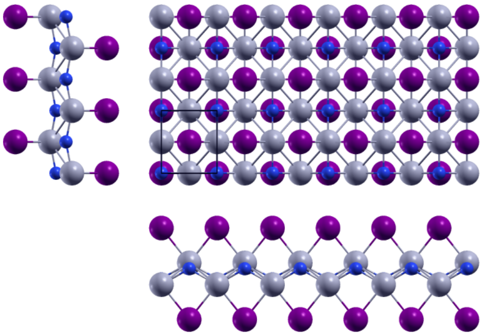

**Table S6.1** Structural parameters: relaxed cell and atomic positions in cartesian coordinates

|  | $x$ [Å] | $y$ [Å] | $z$ [Å] |
|---|---|---|---|
| $\boldsymbol{a}_1$ | 3.533373 | 0.000000 | 0.000000 |
| $\boldsymbol{a}_2$ | 0.000000 | 3.970073 | 0.000000 |
| $\boldsymbol{a}_3$ | 0.000000 | 0.000000 | 25.853267 |
| ● Ti | 1.766687 | 0.000000 | 12.236316 |
| ● I | 0.000000 | 0.000000 | 10.022862 |
| • N | 1.766687 | 1.985036 | 12.608513 |
| ● Ti | 0.000000 | 1.985036 | 13.616950 |
| ● I | 1.766687 | 1.985036 | 15.830404 |
| • N | 0.000000 | 0.000000 | 13.244753 |

# 7. NbIrTe$_4$

### Info and properties

| | |
|---|---|
| **Formula (DB ID)** | NbIrTe$_4$ (ICSD 656451) |
| **Spacegroup** | P$m$ (6) |
| **DFT band gap [meV]** | 36 |
| **DFT inversion strength [meV]** | 161 |
| **No. atoms per unit cell** | 12 |
| **DF2-C09 Binding energy [meV/Å$^2$]** | 27 |
| **rVV10 Binding energy [meV/Å$^2$]** | 32 |

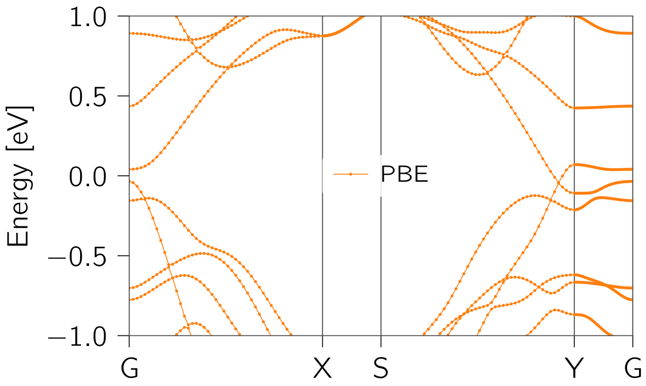

**Figure S7.1** DFT band structure

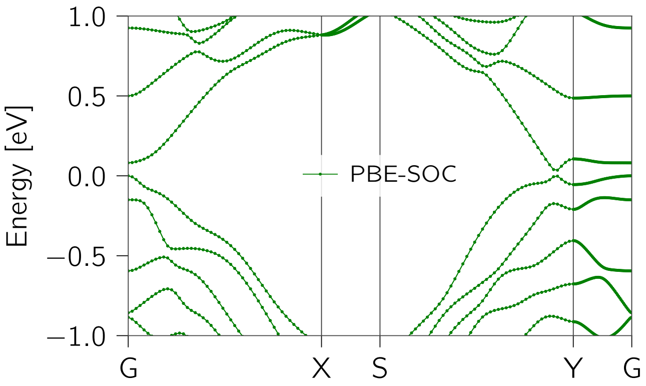

**Figure S7.2** DFT band structure with spin-orbit coupling

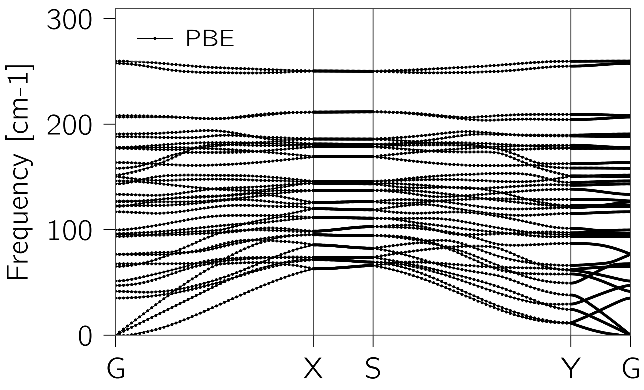

**Figure S7.3** DFPT phonons dispersions

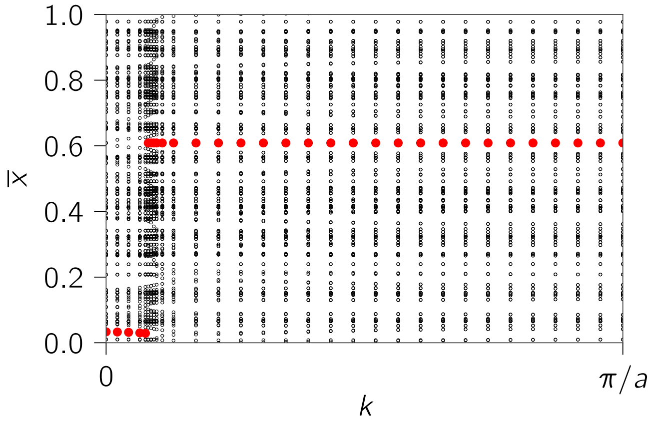

**Figure S7.4** HWCC evolution (empty circles) together with their largest gap (full, red circles)

**Figure S7.5** Orthographic projections

Nb atoms are blue, Te atoms are brown, Ir atoms are dark blue.

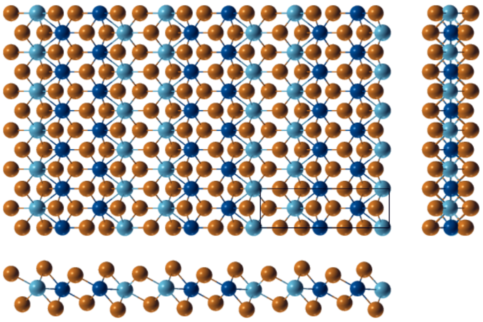

**Table S7.1** Structural parameters: relaxed cell and atomic positions in cartesian coordinates

| | $x$ [Å] | $y$ [Å] | $z$ [Å] |
|---|---|---|---|
| $\boldsymbol{a}_1$ | 3.812967 | 0.000000 | 0.000000 |
| $\boldsymbol{a}_2$ | 0.000000 | 12.600300 | 0.000001 |
| $\boldsymbol{a}_3$ | 0.000000 | −0.000002 | 38.045252 |
| ● Nb | 1.906484 | 9.208256 | −0.096113 |
| ● Te | 0.000000 | 8.527837 | −2.016297 |
| ● Te | 1.906484 | 5.491785 | −1.357496 |
| ● Te | 0.000000 | 2.451313 | −1.886842 |
| ● Te | 1.906484 | 11.776781 | −1.497160 |
| ● Ir | 1.906484 | 3.097544 | −0.043658 |
| ● Nb | 0.000000 | 0.651563 | 0.095884 |
| ● Te | 0.000000 | 4.368115 | 1.357800 |
| ● Te | 0.000000 | 10.683350 | 1.496876 |
| ● Te | 1.906484 | 7.408884 | 1.886963 |
| ● Te | 1.906484 | 1.331702 | 2.016163 |
| ● Ir | 0.000000 | 6.762381 | 0.043881 |

# 8. $TaIrTe_4$

## Info and properties

| | |
|---|---|
| **Formula (DB ID)** | $TaIrTe_4$ (ICSD 73322) |
| **Spacegroup** | P$m$ (6) |
| **DFT band gap** [meV] | 11 |
| **DFT inversion strength** [meV] | 204 |

| | |
|---|---|
| **No. atoms per unit cell** | 12 |
| **DF2-C09 Binding energy** [meV/Å$^2$] | 26 |
| **rVV10 Binding energy** [meV/Å$^2$] | 31 |

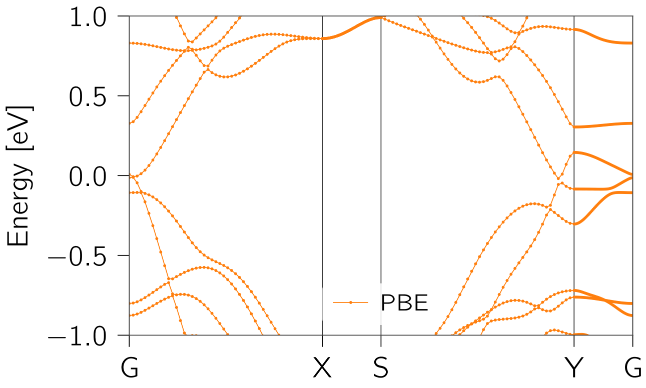

**Figure S8.1** DFT band structure

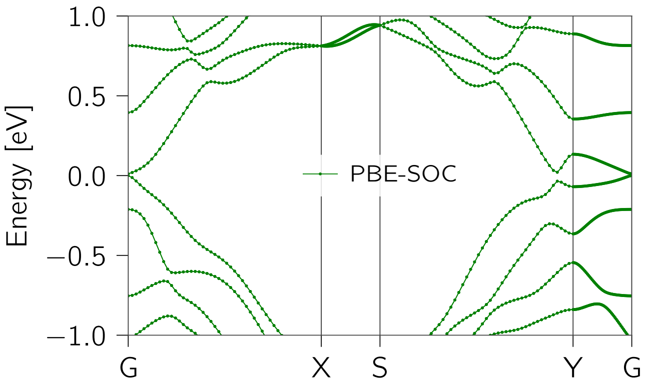

**Figure S8.2** DFT band structure with spin-orbit coupling

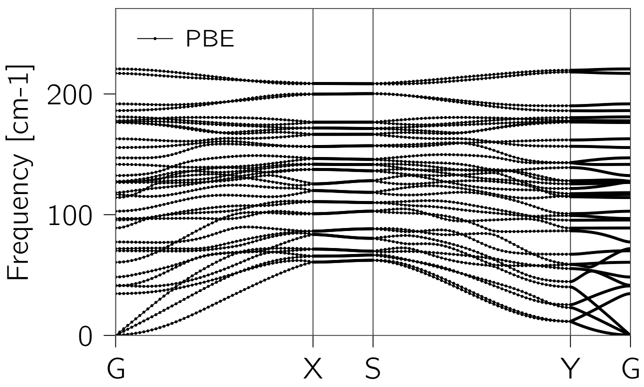

**Figure S8.3** DFPT phonons dispersions

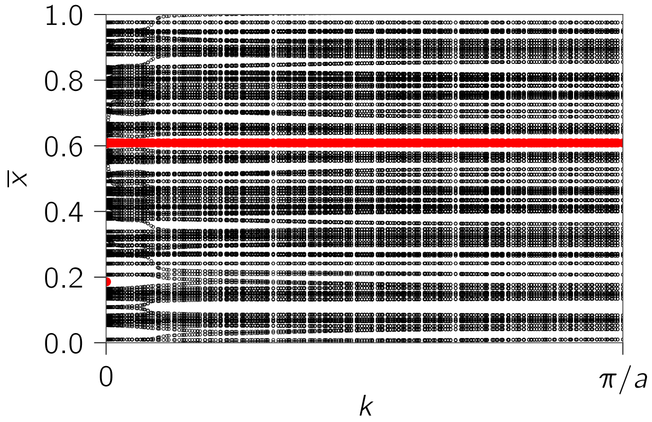

**Figure S8.4** HWCC evolution (empty circles) together with their largest gap (full, red circles)

**Figure S8.5** Orthographic projections

Ta atoms are blue, Te atoms are brown, Ir atoms are dark blue.

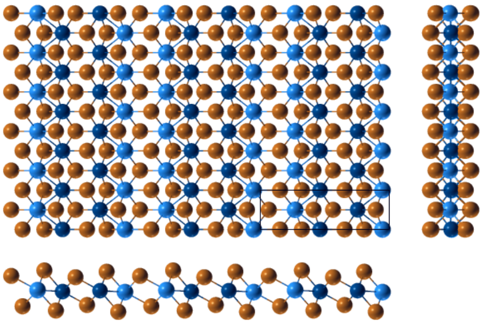

**Table S8.1** Structural parameters: relaxed cell and atomic positions in cartesian coordinates

| | $x$ [Å] | $y$ [Å] | $z$ [Å] |
|---|---|---|---|
| $\boldsymbol{a}_1$ | 3.825507 | 0.000000 | 0.000000 |
| $\boldsymbol{a}_2$ | 0.000000 | 12.578528 | −0.000000 |
| $\boldsymbol{a}_3$ | 0.000000 | 0.000000 | 24.046265 |
| ● Ta | 1.912753 | 9.189664 | 11.910589 |
| ● Te | 1.912753 | 5.482790 | 10.655621 |
| ● Te | 0.000000 | 2.444389 | 10.117132 |
| ● Te | 0.000000 | 8.528962 | 9.991613 |
| ● Te | 1.912753 | 11.761776 | 10.530981 |
| ● Ir | 1.912753 | 3.090984 | 11.965538 |
| ● Ta | 0.000000 | 0.652934 | 12.106504 |
| ● Te | 1.912753 | 7.398290 | 13.900020 |
| ● Te | 1.912753 | 1.313603 | 14.025498 |
| ● Te | 0.000000 | 4.359813 | 13.361527 |
| ● Te | 0.000000 | 10.659346 | 13.486111 |
| ● Ir | 0.000000 | 6.751619 | 12.051611 |

# 9. MoTe$_2$

## Info and properties

| | |
|---|---|
| **Formula (DB ID)** | MoTe$_2$ (COD 2310356) |
| **Spacegroup** | P2$_1$/$m$ (11) |
| **DFT band gap [meV]** | 26 (at 3 % strain) |
| **DFT inversion strength [meV]** | 408 |
| **No. atoms per unit cell** | 6 |
| **DF2-C09 Binding energy [meV/Å$^2$]** | 25 |
| **rVV10 Binding energy [meV/Å$^2$]** | 30 |

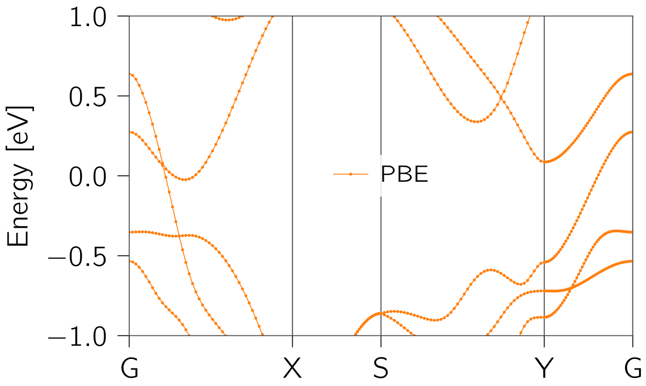

**Figure S9.1** DFT band structure

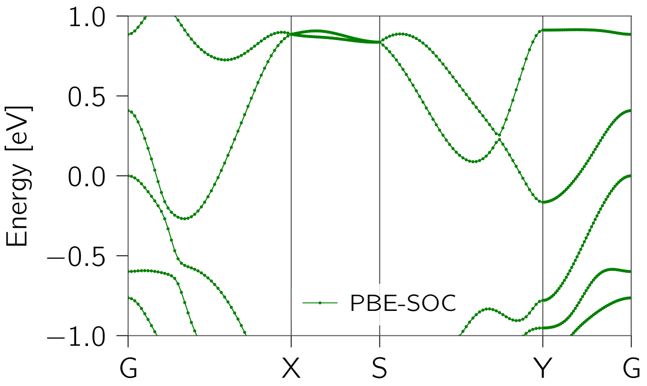

**Figure S9.2** DFT band structure with spin-orbit coupling

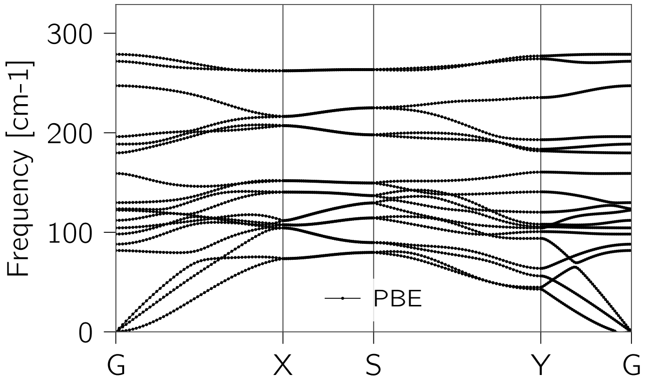

**Figure S9.3** DFPT phonons dispersions

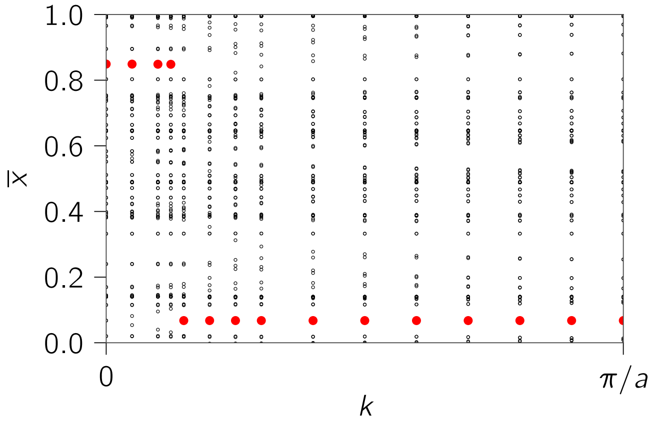

**Figure S9.4** HWCC evolution (empty circles) together with their largest gap (full, red circles)

**Figure S9.5** Orthographic projections

Te atoms are brown, Mo atoms are light blue.

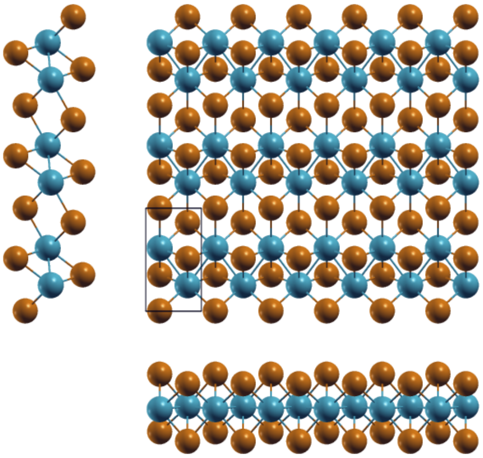

**Table S9.1** Structural parameters: relaxed cell and atomic positions in cartesian coordinates

| | $x$ [Å] | $y$ [Å] | $z$ [Å] |
|---|---|---|---|
| $\boldsymbol{a_1}$ | 3.460070 | 0.000000 | 0.000000 |
| $\boldsymbol{a_2}$ | 0.000000 | 6.378433 | 0.000000 |
| $\boldsymbol{a_3}$ | 0.000000 | 0.000000 | 24.194791 |
| ● Te | 2.595053 | 3.261757 | 14.178702 |
| ● Te | 0.865018 | 2.254486 | 10.016086 |
| ● Te | 0.865018 | 0.012668 | 13.588668 |
| ● Te | 2.595053 | 5.503560 | 10.606125 |
| ● Mo | 2.595053 | 1.605002 | 12.002087 |
| ● Mo | 0.865018 | 3.911189 | 12.192704 |

# 10. $Pd_2HgSe_3$

## Info and properties

**Formula (DB ID)** $Pd_2HgSe_3$ (ICSD 259367)

**Spacegroup** P$\bar{3}m1$ (164)

**DFT band gap [meV]** 0

**DFT inversion strength [meV]** 80

**No. atoms per unit cell** 12

**DF2-C09 Binding energy [meV/Å$^2$]** 61

**rVV10 Binding energy [meV/Å$^2$]** 66

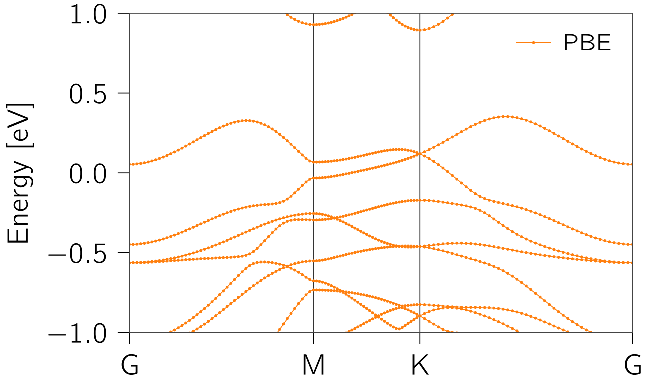

**Figure S10.1** DFT band structure

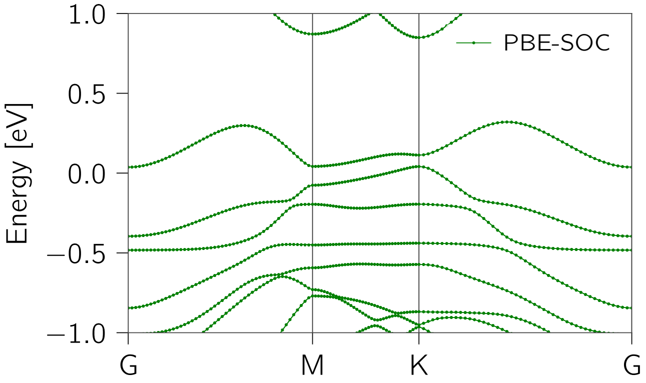

**Figure S10.2** DFT band structure with spin-orbit coupling

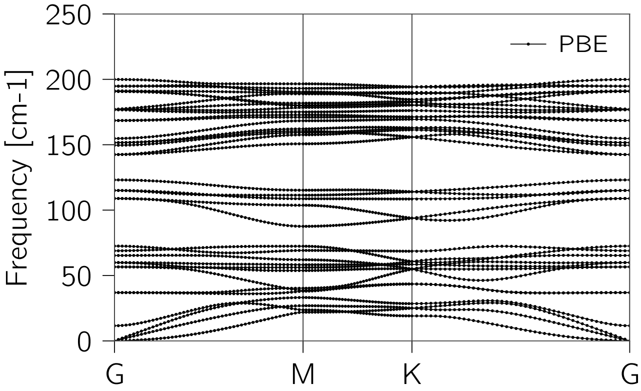

**Figure S10.3** DFPT phonons dispersions

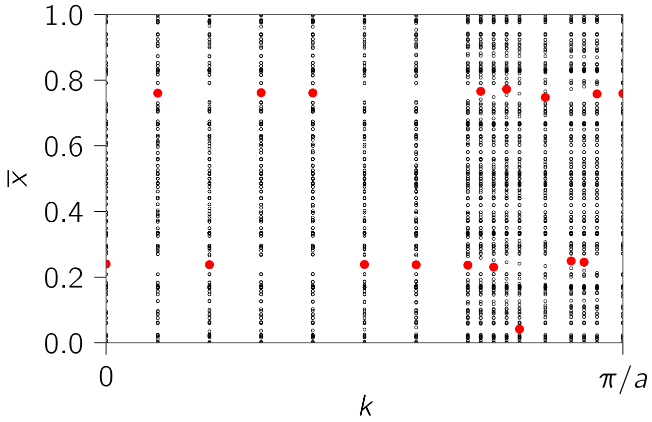

**Figure S10.4** HWCC evolution (empty circles) together with their largest gap (full, red circles)

**Figure S10.5** Orthographic projections

Se atoms are orange, Pd atoms are dark blue, Hg atoms are grey.

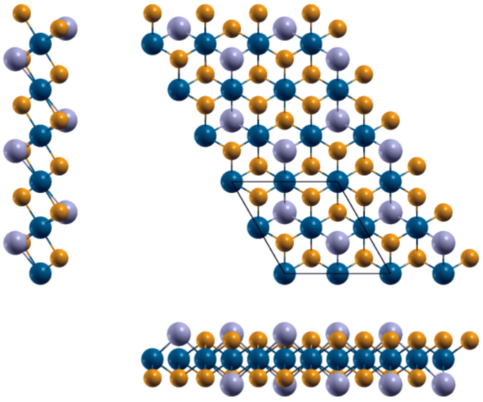

**Table S10.1** Structural parameters: relaxed cell and atomic positions in cartesian coordinates

| | $x$ [Å] | $y$ [Å] | $z$ [Å] |
|---|---:|---:|---:|
| $\boldsymbol{a}_1$ | 7.422649 | 0.000000 | 0.000000 |
| $\boldsymbol{a}_2$ | −3.711325 | 6.428203 | 0.000000 |
| $\boldsymbol{a}_3$ | 0.000000 | 0.000000 | 27.068553 |
| ● Hg | 3.711325 | 2.142734 | 1.761471 |
| ● Hg | 0.000000 | 4.285468 | −1.761471 |
| ● Pd | 0.000000 | 0.000000 | 0.000000 |
| ● Pd | 5.566987 | 3.214101 | 0.000000 |
| ● Pd | 1.855662 | 3.214101 | 0.000000 |
| ● Pd | 3.711325 | 0.000000 | 0.000000 |
| ● Se | 0.000000 | 2.154471 | 1.313237 |
| ● Se | 1.845498 | 5.350967 | 1.313237 |
| ● Se | −1.845498 | 5.350967 | 1.313237 |
| ● Se | 3.711325 | 4.273732 | −1.313237 |
| ● Se | 1.865827 | 1.077236 | −1.313237 |
| ● Se | 5.556822 | 1.077236 | −1.313237 |

# 11. $Pt_2HgSe_3$

## Info and properties

| | | | |
|---|---|---|---|
| **Formula (DB ID)** | $Pt_2HgSe_3$ (ICSD 185808) | **No. atoms per unit cell** | 12 |
| **Spacegroup** | $P\bar{3}m1$ (164) | **DF2-C09 Binding energy [meV/Å$^2$]** | 60 |
| **DFT band gap [meV]** | 149 | **rVV10 Binding energy [meV/Å$^2$]** | 63 |
| **DFT inversion strength [meV]** | 168 | **$G_0W_0$ inversion strength [meV]** | 530 |

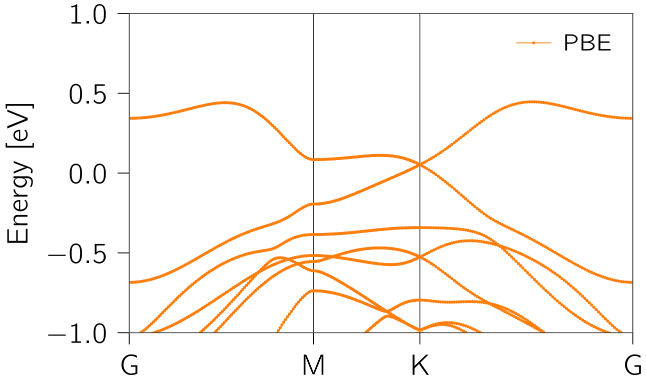

**Figure S11.1** DFT band structure

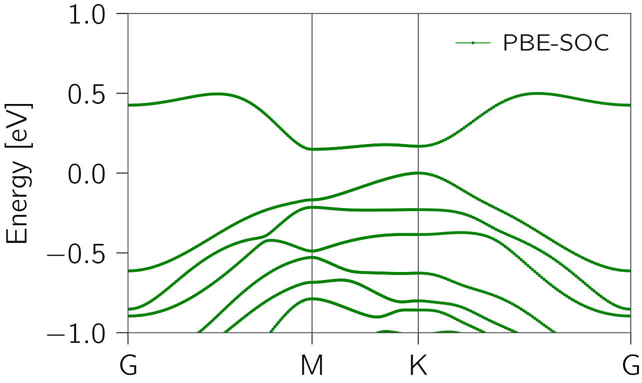

**Figure S11.2** DFT band structure with spin-orbit coupling

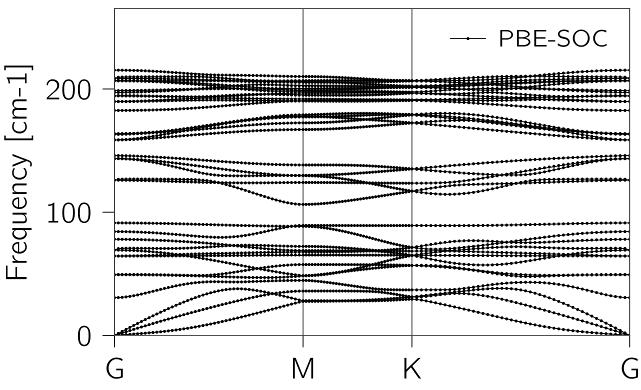

**Figure S11.3** DFPT phonons dispersions

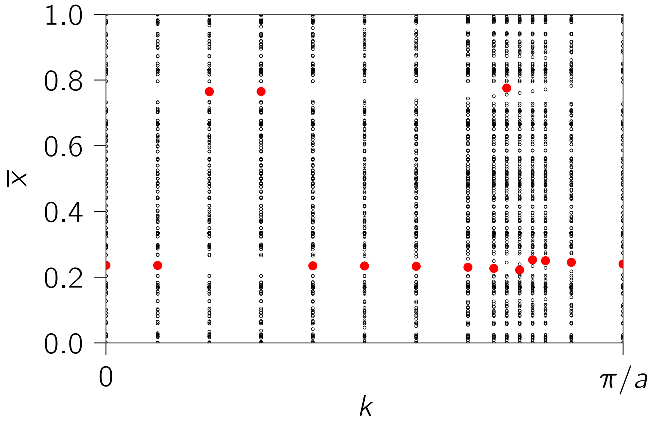

**Figure S11.4** HWCC evolution (empty circles) together with their largest gap (full, red circles)

**Figure S11.5** Orthographic projections

Se atoms are orange, Pt atoms are light grey, Hg atoms are grey.

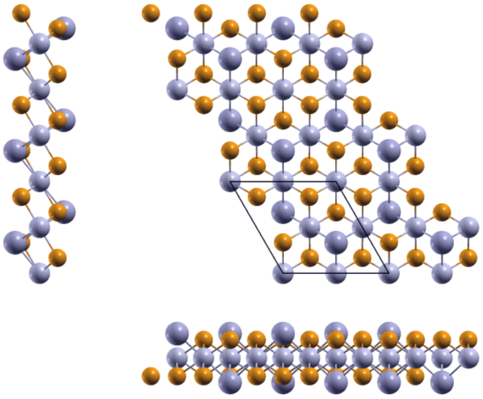

**Table S11.1** Structural parameters: relaxed cell and atomic positions in cartesian coordinates

| | $x$ [Å] | $y$ [Å] | $z$ [Å] |
|---|---|---|---|
| $\boldsymbol{a_1}$ | 7.513867 | 0.000000 | 0.000000 |
| $\boldsymbol{a_2}$ | −3.756933 | 6.507199 | 0.000000 |
| $\boldsymbol{a_3}$ | 0.000000 | 0.000000 | 23.737220 |
| ● Hg | 3.756933 | 2.169067 | 13.595752 |
| ● Hg | 0.000000 | 4.338133 | 10.141468 |
| ● Se | 1.859242 | 5.411567 | 13.153340 |
| ● Se | 0.000000 | 2.191265 | 13.153340 |
| ● Se | −1.859242 | 5.411567 | 13.153340 |
| ● Se | 1.897691 | 1.095633 | 10.583880 |
| ● Se | 3.756933 | 4.315935 | 10.583880 |
| ● Se | 5.616176 | 1.095633 | 10.583880 |
| ● Pt | −0.000000 | −0.000000 | 11.868610 |
| ● Pt | 3.756933 | 0.000000 | 11.868610 |
| ● Pt | 1.878467 | 3.253600 | 11.868610 |
| ● Pt | −1.878467 | 3.253600 | 11.868610 |

# 12. $\mathrm{TaRhTe_4}$

### Info and properties

| | |
|---|---|
| **Formula (DB ID)** | $\mathrm{TaRhTe_4}$ (ICSD 656453) |
| **Spacegroup** | $Pm$ (6) |
| **DFT band gap [meV]** | 65 |
| **DFT inversion strength [meV]** | 215 |
| **No. atoms per unit cell** | 12 |
| **DF2-C09 Binding energy [meV/Å$^2$]** | 26 |
| **rVV10 Binding energy [meV/Å$^2$]** | 31 |

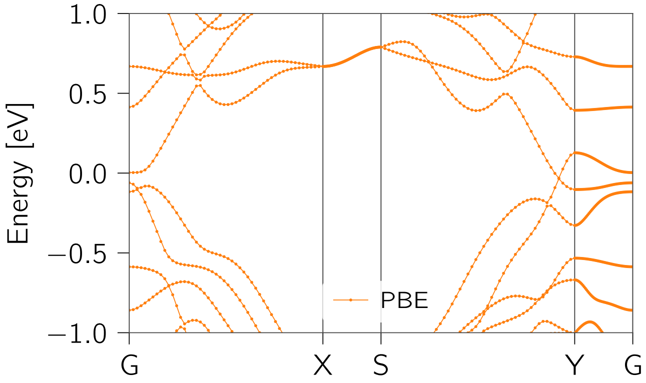

**Figure S12.1** DFT band structure

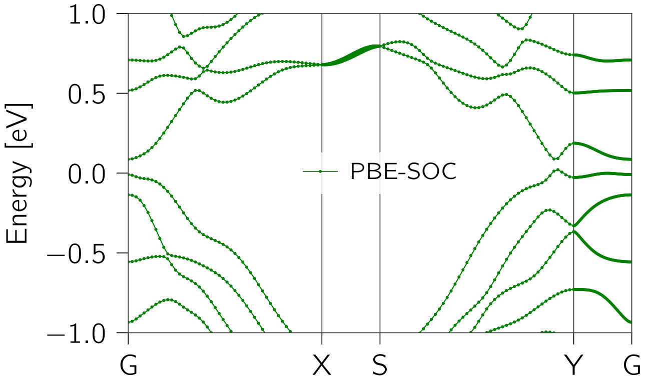

**Figure S12.2** DFT band structure with spin-orbit coupling

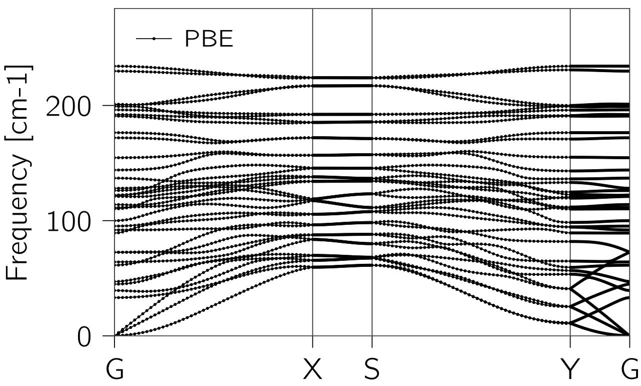

**Figure S12.3** DFPT phonons dispersions

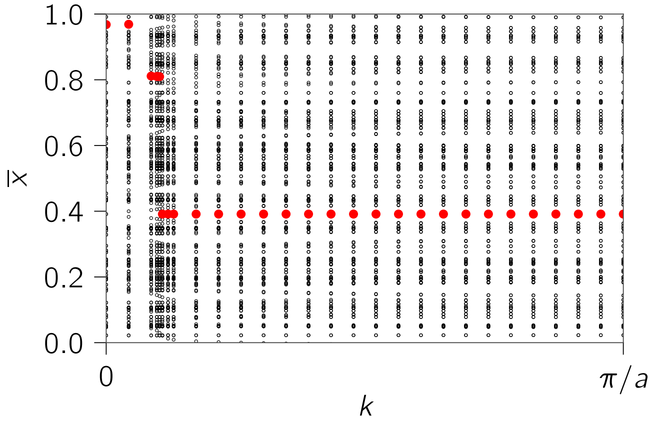

**Figure S12.4** HWCC evolution (empty circles) together with their largest gap (full, red circles)

**Figure S12.5** Orthographic projections

Ta atoms are blue, Te atoms are brown, Rh atoms are dark blue.

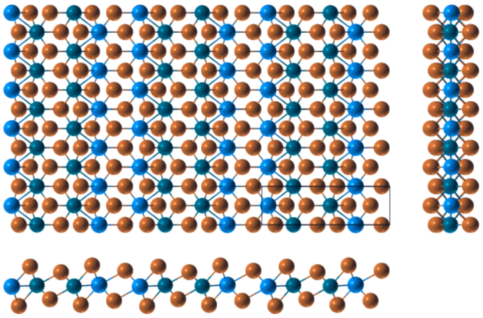

**Table S12.1** Structural parameters: relaxed cell and atomic positions in cartesian coordinates

|  | $x$ [Å] | $y$ [Å] | $z$ [Å] |
|---|---|---|---|
| $\boldsymbol{a_1}$ | 3.798771 | 0.000000 | 0.000000 |
| $\boldsymbol{a_2}$ | 0.000000 | 12.664030 | 0.000000 |
| $\boldsymbol{a_3}$ | 0.000000 | 0.000000 | 38.028106 |
| ● Ta | 0.000000 | 3.394779 | −0.084988 |
| ● Ta | 1.899385 | 12.022434 | 0.084795 |
| ● Te | 1.899385 | 8.258128 | 1.333405 |
| ● Te | 1.899385 | 1.923863 | 1.484899 |
| ● Te | 1.899385 | 4.092027 | −1.999545 |
| ● Te | 0.000000 | 7.159032 | −1.333149 |
| ● Te | 0.000000 | 5.206203 | 1.886254 |
| ● Te | 0.000000 | 0.829308 | −1.485133 |
| ● Te | 0.000000 | 11.325430 | 1.999434 |
| ● Te | 1.899385 | 10.210709 | −1.886161 |
| ● Rh | 0.000000 | 9.536907 | −0.041855 |
| ● Rh | 1.899385 | 5.880232 | 0.042044 |

# 13. $WTe_2$

## Info and properties

**Formula (DB ID)** $WTe_2$ (COD 2310355)
**Spacegroup** $P2_1/m$ (11)
**DFT band gap [meV]** 9 (at 2 % strain)
**DFT inversion strength [meV]** 972

**No. atoms per unit cell** 6
**DF2-C09 Binding energy [meV/Å$^2$]** 30
**rVV10 Binding energy [meV/Å$^2$]** 27

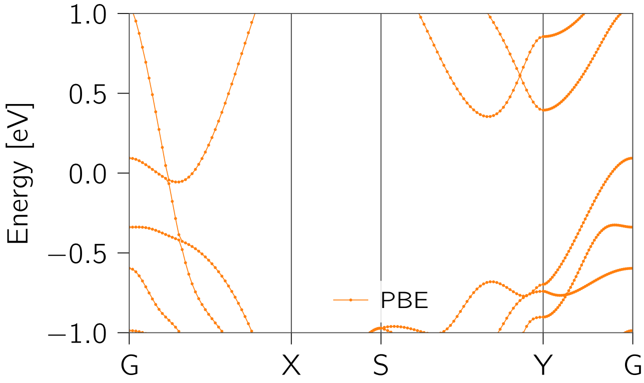

**Figure S13.1** DFT band structure

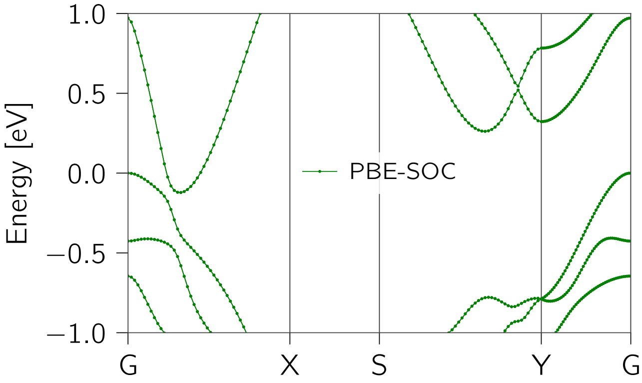

**Figure S13.2** DFT band structure with spin-orbit coupling

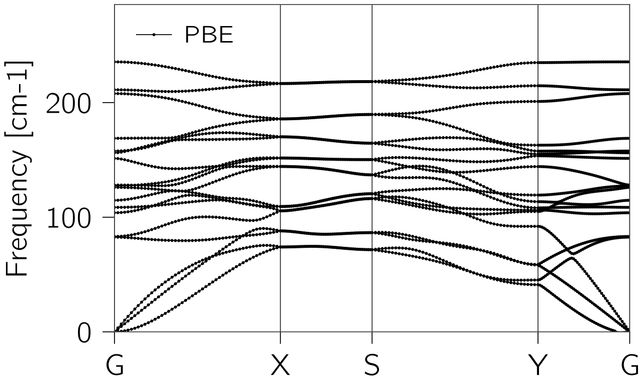

**Figure S13.3** DFPT phonons dispersions

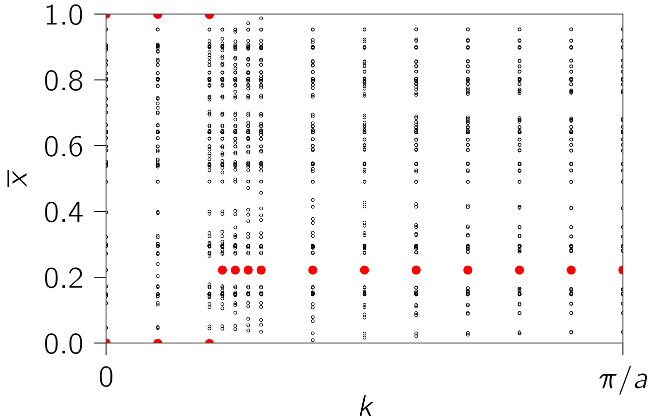

**Figure S13.4** HWCC evolution (empty circles) together with their largest gap (full, red circles)

**Figure S13.5** Orthographic projections

Te atoms are brown, W atoms are blue.

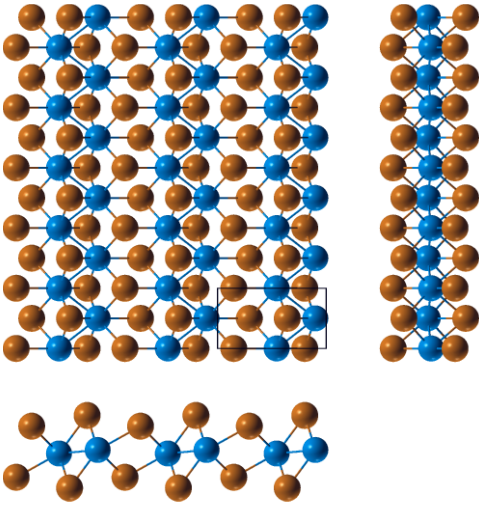

**Table S13.1** Structural parameters: relaxed cell and atomic positions in cartesian coordinates

| | $x$ [Å] | $y$ [Å] | $z$ [Å] |
|---|---|---|---|
| $\boldsymbol{a_1}$ | 3.498051 | 0.000000 | 0.000000 |
| $\boldsymbol{a_2}$ | 0.000000 | 6.327407 | 0.000000 |
| $\boldsymbol{a_3}$ | 0.000000 | 0.000000 | 24.220857 |
| ● Te | 0.000000 | 1.249342 | 10.002354 |
| ● Te | 1.749025 | 4.471362 | 10.624893 |
| ● Te | 1.749025 | 2.271112 | 14.217200 |
| ● Te | 0.000000 | 5.376537 | 13.594651 |
| ● W | 0.000000 | 2.884508 | 12.211794 |
| ● W | 1.749025 | 0.635978 | 12.007757 |

# 14. $In_2ZnS_4$

## Info and properties

**Formula (DB ID)** $In_2ZnS_4$ (ICSD 44637)

**Spacegroup** $P3m1$ (156)

**DFT band gap [meV]** 0

**DFT inversion strength [meV]** 191

**No. atoms per unit cell** 7

**DF2-C09 Binding energy [meV/Å$^2$]** 36

**rVV10 Binding energy [meV/Å$^2$]** 39

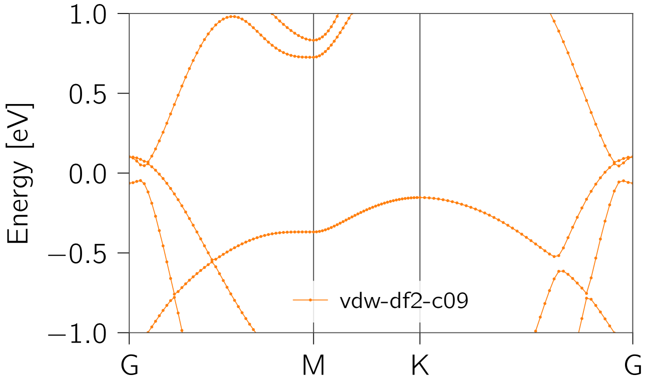

**Figure S14.1** DFT band structure

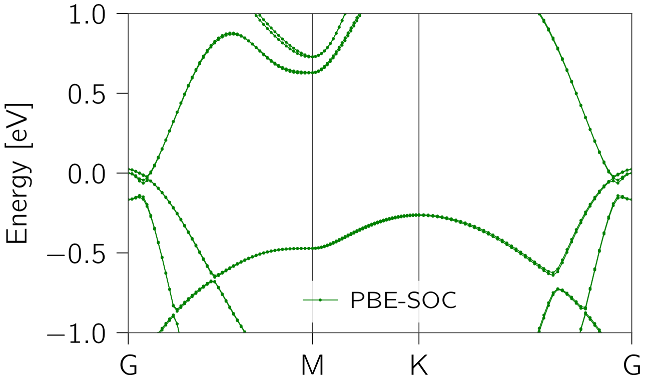

**Figure S14.2** DFT band structure with spin-orbit coupling

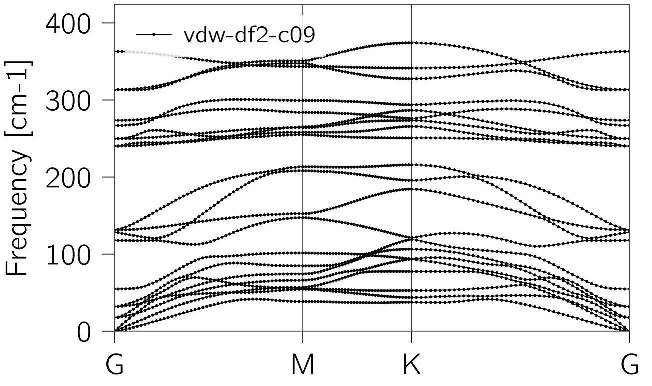

**Figure S14.3** DFPT phonons dispersions

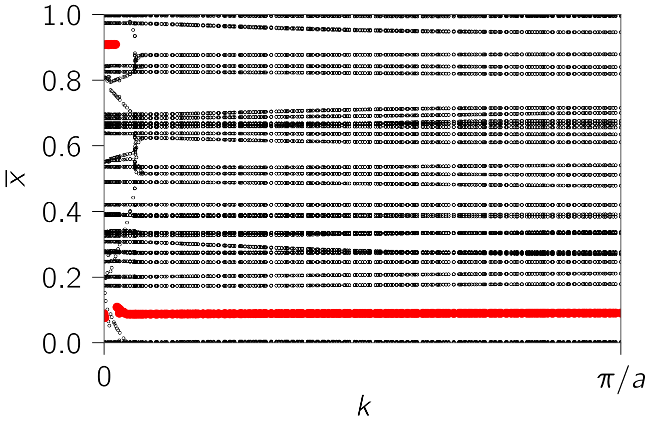

**Figure S14.4** HWCC evolution (empty circles) together with their largest gap (full, red circles)

**Figure S14.5** Orthographic projections

S atoms are yellow, Zn atoms are blue, In atoms are purple.

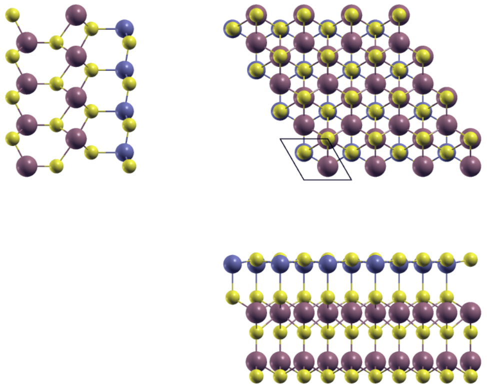

**Table S14.1** Structural parameters: relaxed cell and atomic positions in cartesian coordinates

| | $x$ [Å] | $y$ [Å] | $z$ [Å] |
|---|---|---|---|
| $\boldsymbol{a}_1$ | 3.869260 | 0.000000 | 0.000000 |
| $\boldsymbol{a}_2$ | −1.934630 | 3.350878 | 0.000000 |
| $\boldsymbol{a}_3$ | 0.000000 | 0.000000 | 29.479277 |
| ● In | 1.934630 | 1.116959 | 18.382839 |
| ● S | 1.934630 | 1.116959 | 15.973980 |
| ● In | 1.934630 | 3.350878 | 14.375322 |
| ● S | 1.934630 | 3.350878 | 19.546647 |
| ● Zn | −0.000000 | 2.233918 | 10.428734 |
| ● S | −0.000000 | 2.233918 | 13.138396 |
| ● S | 1.934630 | 1.116959 | 10.057480 |